Available online at www.sciencedirect.com

ScienceDirect

Inorganica Chimica Acta 361 (2008) 1100–1115

Inorganica Chimica Acta

www.elsevier.com/locate/ica

Intermolecular versus intramolecular electron-/atom- ($Cl^{\bullet}$) transfer in heme-iron and copper pyridylalkylamine complexes

H. Christopher Fry [a], Heather R. Lucas [a], Lev N. Zakharov [b], Arnold L. Rheingold [b], Gerald J. Meyer [a,*], Kenneth D. Karlin [a,*]

[a] *The Johns Hopkins University, Department of Chemistry, 3400 North Charles Street, Baltimore, MD 21218, United States*
[b] *University of Delaware, Crystallography Laboratory, Department of Chemistry, Newark, DE 19716, United States*

Received 12 August 2007; accepted 18 August 2007
Available online 25 August 2007

Dedicated to Edward Solomon

Abstract

While outer-sphere electron-transfer reactions come with a firm experimental and theoretical basis, less is known about the redox reactions occurring by atom-transfer. In the present study, relevant reactions occur upon mixing, $(F_8)Fe^{III}(Cl)$ (F_8 is tetrakis(2,6-difluorophenyl)porphyrinate) with a series of $[(L)Cu^{I}]^{+}$ complexes (L are tripodal tetradentate pyridylalkylamine ligands varying in effective chelate ring sizes: TMPA, PMEA, PMAP) to form $(F_8)Fe^{II}$ and $[(L)Cu^{II}(Cl)]^{+}$. The electron-/atom- ($Cl^{\bullet}$) transfer process is characterized by electrochemical measurements as well as UV–Vis, ^1H NMR, and EPR spectroscopies. Stopped-flow UV–Vis spectroscopy in THF indicate the following relative rates (k_{obs}) $[Cu^{I}(pmea)]^{+} > [Cu^{I}(pmap)]^{+} > [Cu^{I}(tmpa)(thf)]^{+}$. However, the redox potentials as related to ΔG° for the reaction, $[E_{1/2}(\text{oxidant}) - E_{1/2}(\text{reductant})]$, predict the trend $[Cu^{I}(tmpa)(CH_3CN)]^{+} > [Cu^{I}(pmea)]^{+} > [Cu^{I}(pmap)]^{+}$. A detailed description of Cu^{I}-to-Cu^{II} structural changes is provided and these likely influence the observed $[(L)Cu^{I}]^{+}/(F_8)Fe^{III}(Cl)$ reaction rates. Analogous chemistry is described for a heme–copper system utilizing a heterobinucleating ligand (^6L), which is comprised of a TMPA like moiety tethered at the 6-position of one of the pyridyl donors to a F_8-like heme. Kinetic/mechanistic insights were obtained from transient absorption spectroscopic monitoring in CH_3CN following photoejection of carbon monoxide from $[(^6L)Fe^{II}(CO)\cdots Cu^{II}(Cl)]$.

Keywords: Copper; Heme; Redox; Electron-/atom-transfer

1. Introduction

In the last few years, we have focused considerable attention on the O_2 and CO chemistry of hemes together with copper ion complexes [1]. Some specific complexes are shown in Scheme 1, where either as individual components, i.e., 1:1 mixtures of $[Cu^{I}(tmpa)(CH_3CN)]^{+}$ ($^{\mathbf{tmpa}}\mathbf{2}$) and $(F_8)Fe^{II}$ (**1**), or by using the binucleating ligand complex $[^6LFe^{II}\cdots Cu^{I}]^{+}$, we have shown that reaction of O_2 with these reduced $Fe^{II}\cdots Cu^{I}$ mixtures/assemblies (Scheme 1) first leads to heme-superoxo transients (e.g., $Fe^{III}–(O_2^{-})\cdots Cu^{I}$ species) which then react further to form peroxo-bridged $Fe^{III}–(\mu\text{-}\eta^2:\eta^1\text{-}O_2^{2-})–Cu^{II}$ complexes [1–3]. The latter have been characterized in detail, in connection with modeling the active site chemistry of heme–copper oxidases which reduce O_2 to water [1,4,5]. Reduced complexes are also known to bind carbon monoxide; $[(^6L)Fe^{II}\cdots Cu^{I}]^{+}$ (Scheme 1) ligates CO at one or both metal centers. The heme mono-carbonyl, $[(^6L)Fe^{II}(CO)\cdots Cu^{I}]^{+}$, has proven to be a useful tool in studying photoinduced reaction dynamics [6–8].

In earlier work [9], we reported what turned out to be a useful alternative synthesis of $(F_8)Fe^{II}$ (**1**) via introduction of $[Cu^{I}(tmpa)(CH_3CN)]^{+}$ ($^{\mathbf{tmpa}}\mathbf{2}$) to $[(F_8)Fe^{III}(Cl)]$ (**1′-Cl**) in

---

[*] Corresponding authors.
E-mail address: karlin@jhu.edu (K.D. Karlin).

0020-1693/$ - see front matter © 2007 Elsevier B.V. All rights reserved.
doi:10.1016/j.ica.2007.08.016

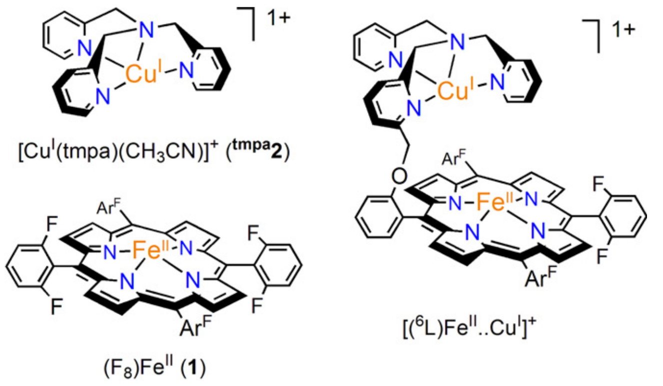

Scheme 1.

deaerated toluene (Scheme 2). On the basis of classical inorganic chemistry redox reaction considerations, it seems likely that this process occurs by an inner-sphere electron-transfer mechanism involving a bridging chloride, i.e., there is formally a net transfer of a chlorine atom (Cl$^\bullet$) from heme to copper. Here, this fundamentally interesting process is studied further by examination of related chemical systems which involve both intra- and inter-molecular electron-/atom- (Cl$^\bullet$) transfer reactions.

In addition to [Cu^I(tmpa)(CH$_3$CN)]$^+$ ($^{\mathbf{tmpa}}$**2**), a related series of pyridylalkylamine tripodal tetradentate ligand–copper complexes ($^{\mathbf{R}}$**2**), [Cu^I(pmea)]$^+$, [Cu^I(pmap)]$^+$, and [Cu^I(tepa)]$^+$ (Scheme 2), have been employed. This allows for a systematic examination of how changes in the nature of the ligand influence electron-/atom-transfer chemistry while employing the same oxidant, (F$_8$)Fe^{III}(Cl) (**1′-Cl**). It has been presented elsewhere that systematically expanding the five-membered chelate rings by one carbon atom, such as in the ligand series TMPA → PMEA → PMAP → TEPA, significantly changes the coordination geometry (based on X-ray diffraction studies) around the copper(II) ion center in complexes derived from these, while there are also significant changes in Cu$^{II/I}$ redox potentials [10–12]. Therefore, study of these systems affords the ability to observe the process of electron-/atom- (Cl$^\bullet$) transfer as a function of copper coordination geometry and redox properties.

The binucleating ligand ^{6}L was also employed here in order to provide further insight into the electron-/atom- (Cl$^\bullet$) transfer reactions and for comparison of intra- versus inter-molecular reaction chemistry. Our previous success in utilizing ^{6}L to provide the framework necessary to stabilize bridging O$_2$ intermediates as Fe^{III}–(O$_2$$^{2-}$)–Cu^{II} complexes (*vide supra*) [3,13] appears ideal for probing the reactions

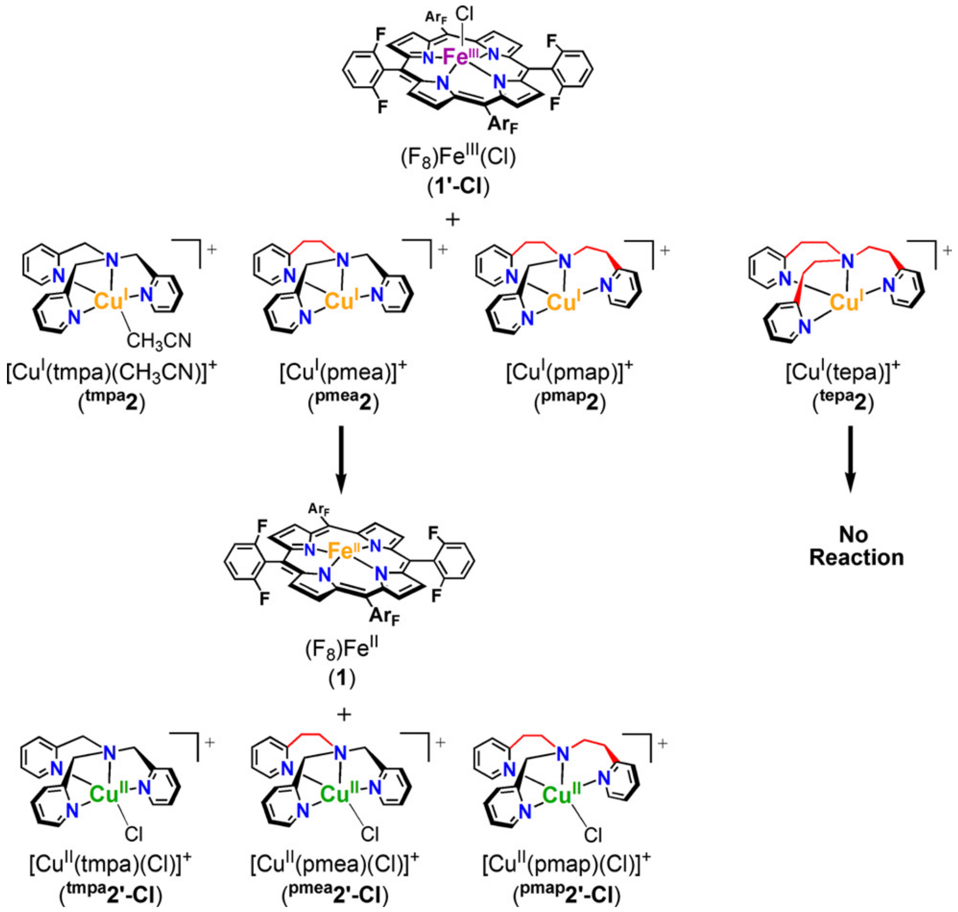

Scheme 2.

involving an intramolecular chlorine atom transfer with possible bridging Cl^- intermediate. For this purpose, we have in fact been able to generate $[(^6L)Fe^{III}(Cl)\cdots Cu^I]^+$ ($\mathbf{3^{FeCl}}$) or species derived from it (as outlined in Section 3) and can indeed observe intramolecular redox-atom transfer.

Various analytical techniques including ^1H NMR, EPR, electrochemistry, and UV–Vis spectroscopy have been employed to characterize this electron-/atom- ($Cl^\bullet$) transfer process as a function of copper–ligand environment. In addition, the relative rates of this process have been examined by transient absorption spectroscopy. In summary, we report how changes in the nature of the ligand influence LCu^I/LCu^{II} geometries, redox properties, the driving force (ΔG°) and rate of electron-/atom- ($Cl^\bullet$) transfer from heme to copper. We also report a novel means by which $Cl^\bullet$ atom transfer reactions can be photoinitiated.

2. Experimental

2.1. Materials and methods

All reagents were purchased from commercial sources. All air sensitive compounds were synthesized utilizing Schlenk techniques. Tetrahydrofuran solvent was purified using MBraun alumina solvent purification columns. Acetonitrile was dried and distilled over calcium hydride under an argon atmosphere. The air-sensitive compounds and dried, degassed (purging with argon 1 h) solvents were introduced into an MBraun Labmaster 130 dry box. UV–Vis absorption spectra were obtained using a Hewlett–Packard 8452A or a Hewlett–Packard 8453 diode array spectrophotometer. Low temperature measurements (−80 to 0 °C) were made using a Neslab ULT-95 controller by circulating methanol through a two window optical dewar as previously described [3,14]. UV–Vis spectroscopic samples of $(F_8)Fe^{III}(Cl)$ in dried, air-free CH_3CN were added to samples of $[(L)Cu^I]B(C_6F_5)_4$ in equimolar concentrations in the dry box and transferred to a 10 mm Quark Glassware Schlenk quartz cuvette equipped with a 14/20 rubber septum. X-band electron paramagnetic resonance (EPR) spectroscopic studies were performed using a Bruker EMX magnet operating at a frequency of 9.4 GHz; 1–2 mM samples were prepared in 50:50 CH_3CN:toluene and frozen in liquid N_2 before cooling further to 12–16 K for spectroscopic measurements. NMR spectroscopy was performed using a Varian 400 MHz instrument. All spectra were recorded at room temperature in 5 mm o.d. NMR tubes. Reported spectra were generated using MestReC NMR processing software. Matrix-assisted laser desorption ionization time-of-flight (MALDI TOF) mass spectra were recorded with a Kratos Analytical Kompact MALDI 4 mass spectrometer equipped with a 337 nm nitrogen laser (20 kV extraction voltage). No matrix was necessary for the MALDI-TOF samples as the presence of porphyrin ligand itself proved to be sufficient for laser desorption.

2.2. Syntheses of complexes

The following ligand–metal complexes have been previously synthesized and characterized: $[Cu^I(CH_3CN)_4]$-$B(C_6F_5)_4$ [22], $[Cu^I(tmpa)(CH_3CN)]B(C_6F_5)_4$ ($\mathbf{^{tmpa}2}$) [15], $[Cu^I(pmea)]B(C_6F_5)_4$ ($\mathbf{^{pmea}2}$) [16], $[Cu^I(pmap)]B(C_6F_5)_4$ ($\mathbf{^{pmap}2}$) [16], $(F_8)Fe^{III}(Cl^\bullet)$ (**1′-Cl**) [17] and $(^6L)Fe^{II}$ [3]. The ligands TEPA [11] and ^6L [13] was synthesized as previously described.

2.2.1. Synthesis of $[Cu^I(tepa)]B(C_6F_5)_4$ ($^{tepa}2$)

$[Cu^I(CH_3CN)_4]B(C_6F_5)_4$ (300 mg, 0.33 mmol) was placed in a 100 mL Schlenk flask equipped with a stirbar. To this solid, TEPA (110 mg, 0.33 mmol) dissolved in dried and deaerated diethyl ether was added under an Ar atmosphere. The resulting yellow solution was stirred for 30 min. Dried and deaerted heptane (100 mL) was added to precipitate the complex. After stirring for 1 h, the supernatant was decanted. The remaining yellow oily solid was dissolved again in dried and dearated diethyl ether (10 mL) and precipitated with deaerated heptane (100 mL). The resulting solid was placed in vacuo to yield 295 mg (83%) of a yellow powder. Elemental Analysis: Calculated: C, 50.28; H, 2.25; N, 5.21. Experimental: C, 50.11; H, 1.97; 5.14.

2.2.2. Synthesis of $^6LFe^{III}(Cl)\cdot 2H_2O\cdot CH_2Cl_2$

The ligand ^6L (900 mg) was dissolved in dimethylformamide (150 mL) under Ar and placed in a 250 mL, three-neck round bottom flask equipped with a stirbar and condenser. This was then attached to a Schlenk line. The solution was purged with argon for 30 min and was then heated until the flask was warm to the touch. At this time, $Fe^{II}Cl_2\cdot 4H_2O$ was added to the solution under positive argon flow. After 2.5 h, the reaction was expose to air and was set to cool to room temperature. The DMF was removed by rotary evaporation. The crude product was dissolved in methylene chloride and was then added to a stirring solution of saturated NaOH (700 mL). This mixture was then stirred overnight. The methylene chloride layer was then dried over sodium sulfate and adsorbed onto alumina. Purification by column chromatography (1:1 hexanes/ethyl acetate) yielded$(^6L)Fe^{III}(OH)$. This product was then dissolved in 100 mLCH_2Cl_2 and trimethylsilylchloride (TMS-Cl, 1.0 mL) was added. After 3 h, the volatiles were removed by rotary evaporation, yielding a purple product. UV–Vis (CH_3CN): Soret, 412 nm; α, 504, 572, 630 nm. MALDI-TOF MS: 1131.0 *m*/*z*. Elemental Analysis: Calculated: C, 61.43; H, 3.71; N, 8.96. Experimental: C, 61.61; H, 3.70; N, 8.34.

2.2.3. Synthesis of $[(^6L)Fe\cdots(Cl)\cdots Cu]B(C_6F_5)_4$ (3)

In a 150 mL Schlenk flask, $(^6L)Fe^{III}(Cl)$ (100 mg, 0.080 mmol) and $[Cu^I(CH_3CN)_4]B(C_6F_5)_4$ (78 mg, 0.086 mmol) were dissolved in 10 mL of tetrahydrofuran. The solution was stirred for 1 h. During this time, 100 mL of heptane (dried and distilled) was bubbled with argon and this was added to the stirring solution which resulted in precipitation of a purple solid. The heptane was removed via cannula and the resulting purple solid was dried *in vacuo*. UV–Vis (CH_3CN, −40 °C) Soret, 424 nm; α, 528 nm; (THF, −40 °C) Soret, 424 nm; a, 541 nm. MALDI-TOF MS: 1193.0 *m*/*z*. Elemental Analysis: Calculated: C, 54.76; H, 2.11; N, 5.87. Experimental: C, 54.37; H, 2.28; N, 5.52.

2.3. Electrochemistry

Cyclic voltammetry was carried out using a Bioanalytical Systems BAS-100B electrochemistry analyzer. The cell consisted of a 25 mL three-necked round bottom flask equipped with rubber septa. Each neck possessed one of the following: a glassy carbon working electrode, a saturated calomel reference electrode equipped with a salt bridge necessary for organic solvents or a $Ag/AgPF_6$ electrode in CH_3CN, and a platinum wire as the auxiliary electrode. Ferrocene was used as an external standard. The measurements were performed at room temperature under an argon atmosphere in CH_3CN solutions, containing 100 mM tetrabutylammonium hexafluorophosphate electrolyte, using 1–3 mM complex concentrations.

2.4. Transient absorption spectroscopy

Transient absorbance measurements were performed using an Nd:YAG (Continuum Surelite III) laser on a previously described apparatus [18]. Samples of $[(^6L)Fe^{II}(CO)\cdots Cu^{II}(Cl)]B(C_6F_5)_4$ (**5**) were prepared *in situ* upon dissolution of $[(^6L)Fe\cdots(Cl)\cdots Cu]B(C_6F_5)_4$ (**3**) in acetonitrile and saturating with CO(g). The samples were irradiated with 532 nm pulsed light at 2–10 mJ/cm^2 and protected from the probe beam with appropriate UV filters. For full transient absorption spectra, 0.5–3 μM samples were used in a 1.0 cm pathlength cuvette and kinetic traces were monitored from 320 to 650 nm with varying steps (every 5–10 nm) averaging 40 transients per wavelength.

The CO concentration was varied in all solvents studied in order to determine bimolecular rate constants, k_{CO} ($M^{-1}\ s^{-1}$). CO was varied (1–10 mM in 1 mM steps) as previously described using a gas mixer (N_2 was used as the supporting inert gas) [19]. Four wavelengths were monitored in the Soret region averaging 60–120 transients per wavelength and the observed rate constants were averaged at each CO concentration studied. Plotting the observed rate constants, k_{obs} versus CO concentration resulted in a linear fit. The slope corresponds to the bimolecular rate of recombination, k_{CO} ($M^{-1}\ s^{-1}$).

2.5. Stopped-flow spectroscopy

Time-resolved UV–Vis spectroscopy was performed using a Hi-Tech Scientific SF-40 stopped-flow apparatus equipped with a low temperature dewar allowing temperature variation from 183 to 298 K. The stopped-flow apparatus was coupled to a J&M Tidas diode-array spectrophotometer equipped with J&M Tidas Spectralys 200 software. All kinetic processes were analyzed using the first-order integrated rate law with ORIGIN 6.1 software. Samples were prepared in the dry box and transferred to an additional funnel designed to attach to the stopped-flow apparatus in order to load the syringes under an inert atmosphere. The apparatus used was similar to that previously employed and it was used in a like manner [20].

2.6. X-ray diffraction

X-ray quality crystals of $[(^6L)Fe^{III}(Cl)\cdots Cu^{II}(Cl)]B(C_6F_5)_4$ (**4**) were obtained from dissolving $[(^6L)Fe\cdots(Cl)\cdots Cu]B(C_6F_5)_4$ (**3**) in $MeOH/CH_2Cl_2$ (<1 mL) and layering with heptane (5 mL) in a 5 mm o.d. NMR tube under Ar. After 4-days purple crystals were obtained. The X-ray data was obtained and analyzed at the University of Delaware (laboratory of A.L. Rheingold). The structure was solved using direct methods, completed by subsequent difference, Fourier syntheses, and refined by full-matrix least-squares procedures. All non-hydrogen atoms were refined with anisotropic displacement coefficients, and the hydrogen atoms were treated as idealized contributions. All software and sources of the scattering factors are contained in the SHELXTL (5.1) program library (G. Sheldrick, Siemens XRD, Madison, WI). Solvent molecules, CH_2Cl_2 and CH_3OH, in the crystal structure were highly disordered and were treated by SQUEEZE [21]. Correction of the X-ray data by SQUEEZE, 210 electron/cell, was close to the required values 204 electron/cell for four CH_2Cl_2 and two CH_3OH in the full unit cell.

3. Results and discussion

3.1. Synthesis

The syntheses of the mononuclear copper(I) species ($^{\mathbf{R}}\mathbf{2}$), $[Cu^I(tmpa)(CH_3CN)]B(C_6F_5)_4$ ($^{\mathbf{tmpa}}\mathbf{2}$), $[Cu^I(pmea)]B(C_6F_5)_4$ ($^{\mathbf{pmea}}\mathbf{2}$), $[Cu^I(pmap)]B(C_6F_5)_4$ ($^{\mathbf{pmap}}\mathbf{2}$), are described in a separate publication [16]; that for $[Cu^I(tepa)]B(C_6F_5)_4$ ($^{\mathbf{tepa}}\mathbf{2}$) (Scheme 2) is given in the Experimental Section. The cupric chloride species ($^{\mathbf{R}}\mathbf{2'}$**-Cl**), $[Cu^{II}(tmpa)(Cl)]B(C_6F_5)_4$ ($^{\mathbf{tmpa}}\mathbf{2'}$**-Cl**), $[Cu^{II}(pmea)(Cl)]B(C_6F_5)_4$ ($^{\mathbf{pmea}}\mathbf{2'}$**-Cl**), and $[Cu^{II}(pmap)(Cl)]B(C_6F_5)_4$ ($^{\mathbf{pmap}}\mathbf{2'}$**-Cl**), were produced *in situ* upon addition of the respective cuprous salt to the heme–chloride complex **1′-Cl** in acetonitrile (CH_3CN) or tetrahydrofuran (THF) solvent under argon (Scheme 2). With the presence of such strong heme chromophores, a typical color change from brown to bright red is visible on the bench-top upon reduction of the ferric tetraarylporphyrins to their ferrous counterparts.

Procedures for metallation of the free base porphyrins, F_8 and ^6L, with $Fe^{II}Cl_2 \cdot 4H_2O$ to produce the corresponding $(F_8)Fe^{III}Cl$ (**1′-Cl**) [17] (Scheme 2) and $(^6L)Fe^{III}OH$ [3] ferric compounds were previously published; these complexes are already fully characterized. The target ferric chloride species of the heterobinucleating ligand ^{6}L, (^{6}L)Fe^{III}(Cl) with empty TMPA moiety, was produced upon washing (^{6}L)Fe^{III}(OH) with a mild acid, trimethylsilylchloride (TMS-Cl); treatment with a stronger acid, such as HCl, results in cleavage of the heterobinucleating ligand ether linkage.

Introduction of [Cu^{I}(CH$_3$CN)$_4$]B(C$_6$F$_5$)$_4$ [22] to metallate the non-heme moiety of (^{6}L)Fe^{III}(Cl) in deaerated THF solvent also results in chloride transfer as can be observed macroscopically. However, the electron-/atom- (Cl$^{\cdot}$) transfer from iron to copper is incomplete leading to a mixture of [(^{6}L)Fe$^{II}\cdots$Cu^{II}(Cl)]$^+$ (**3^{CuCl}**) and [(^{6}L)Fe^{III}(Cl)$\cdots$Cu^{I}]$^+$ (**3^{FeCl}**); this electron-/atom- (Cl$^{\cdot}$) transfer phenomena will be described throughout in detail. The equilibrium position (Scheme 3), **3^{CuCl}** versus **3^{FeCl}**, is dependent on solvent interaction and concentration; therefore, the isolated solid and apparent mixture is from here on referred to as [(^{6}L)Fe$\cdots$(Cl)$\cdots$Cu]$^+$ (**3**).

3.2. X-ray crystallography of [(^{6}L)Fe^{III}(Cl)$\cdots$Cu^{II}(Cl)]$^+$ (4)

The attempted crystallization of [(^{6}L)Fe$\cdots$Cl$\cdots$Cu]$^+$ (**3**) in a MeOH/CH$_2$Cl$_2$/heptane solvent mixture led to crystals of a disproportionation product, [(^{6}L)Fe^{III}(Cl)$\cdots$Cu^{II}(Cl)]$^+$ (**4**), which was characterized by X-ray crystallography, Fig. 1. This compound is relevant in order to deduce structural aspects of the heme–Cu assembly being studied, especially as concerns the copper ion environment. The heme portion of **4** follows what is typically expected of five-coordinate high-spin (porphyrinate)Fe^{III}–X complexes [17,23,24], with **4** having an average Fe–N distance of 2.06 Å and with the iron ion positioned 0.46 Å out of the heme plane. The copper moiety of **4** exhibits a distorted square pyramidal (sp) geometry (also see discussion below). A distinctive aspect of the present structure is that the tethered pyridyl moiety containing the cupric ion swings away from the heme, possibly as a result of the two chloride anions repelling one another or perhaps as a preferential crystal and crystal packing arrangement.

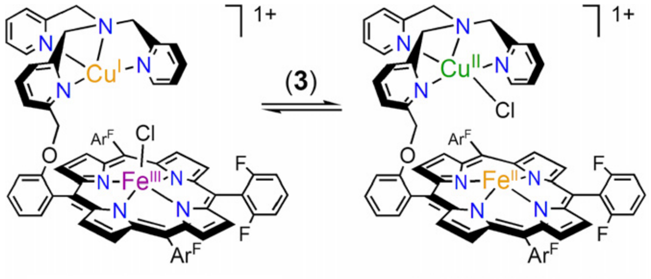

[(^{6}L)Fe^{III}(Cl)..Cu^{I}]$^+$ (**3^{FeCl}**)

[(^{6}L)Fe^{II}..Cu^{II}(Cl)]$^+$ (**3^{CuCl}**)

Scheme 3.

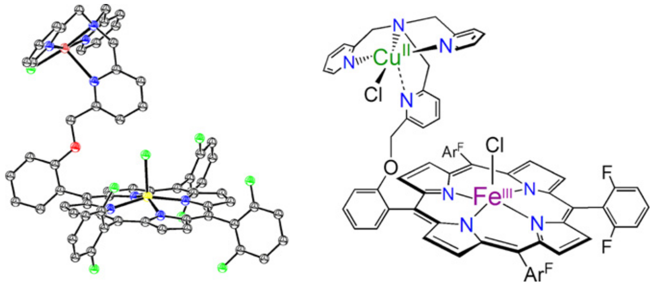

Fig. 1. ORTEP representation and drawing based on the X-ray structure of [(^{6}L)Fe^{III}(Cl)$\cdots$Cu^{II}(Cl)]$^+$ (**4**). See text for further discussion.

3.3. Relevant structural aspects of copper(I/II) complexes

Geometric variation of the ligand environment around the copper ion like presented here is of fundamental interest for a further understanding of the various factors involved when converting copper(I) to copper(II) via electron-/atom- (Cl$^{\cdot}$) transfer reactions. In addition, the geometry change which results upon reduction of (F$_8$)Fe^{III}(Cl) (**1′-Cl**) to (F$_8$)Fe^{II} (**1**) contributes to this process, but we employed **1′-Cl** as our single oxidizing species to minimize variables that may alter our understanding of these reactions.

When copper is oxidized from copper(I) to copper(II) in typical non-protein ligand environments, a drastic geometric change from the ideal four coordinate tetrahedral cuprous species (3d^{10}) to a five coordinate square-based pyramidal (sp) or trigonal bipyramidal (tbp) cupric (3d^{9}) species most often occurs. For [Cu^{I}(tmpa)(CH$_3$CN)]$^+$ (**^{tmpa}2**), ^{1}H NMR investigations have indicated an internal fluxional process where dissociation and re-association of a pyridyl arm occurs rapidly. The tetradentate ligand is essentially coordinated in an N$_3$ fashion with an additional solvent ligand present (Scheme 4) [20,25,26]. Thus, the structural rearrangement necessary to convert **^{tmpa}2** to the perfect trigonal bipyramidal **^{tmpa}2′-Cl** complex is quite drastic (Scheme 4). On the contrary, much less dramatic geometric changes occur in the cases of [Cu^{I}(pmea)]$^+$ (**^{pmea}2**) and [Cu^{I}(pmap)]$^+$ (**^{pmap}2**), as all of the pyridyl nitrogens are coordinated to the cuprous metal center in solution [11]. The addition of a chloride anion by **1′-Cl** to **^{pmea}2** and **^{pmap}2** expands the ligand–metal coordination number from four to five, in forming their corresponding cupric analogues, **^{pmea}2′-Cl** and **^{pmap}2′-Cl**, as there is not

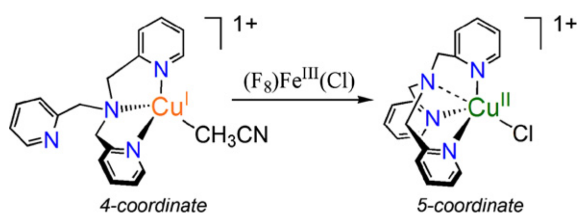

Scheme 4.

a solvent molecule coordinated in the Cu^{I} ion complex [11,16].

Based on the structural index parameter τ, defined by Reedijk and Addison [27] to describe pentacoordinate complexes, a perfect tbp geometry has a τ value of 1, like $[Cu^{II}(tmpa)(Cl)]^{+}$, and sp coordination has a τ value of 0, similar to that of $[Cu^{II}(tepa)(Cl)]^{+}$, Scheme 5 [28]. The TEPA framework of $[Cu^{II}(tepa)(Cl)]^{+}$ houses a geometry closest to the ideal square planar geometry desired by $3d^{9}$ cupric systems. The sp cupric complexes $^{\mathbf{pmea}}\mathbf{2'\text{-}Cl}$ and $^{\mathbf{pmap}}\mathbf{2'\text{-}Cl}$ have τ values of 0.12 and 0.08, respectively [11]. Similarly, the τ value for the copper(II)–chloride moiety of the heme–copper complex $[(^{6}L)Fe^{III}(Cl)\cdots Cu^{II}(Cl)]^{+}$ (**4**) is 0.19, where the axial ligand is the pyridyl group comprising the linker between the heme and copper-chelate in ^{6}L; Cu–N = 2.32 Å. This τ value is drastically different than the mononuclear analogue $^{\mathbf{tmpa}}\mathbf{2'\text{-}Cl}$. However, we previously established that cupric chloride TMPA analogs possessing 6′-substituents on one of the pyridyl groups begin to distort their coordination geometry from perfect tbp to sp [29]. The square-based pyramidal copper geometry of the copper(II)–chloride moiety of $[(^{6}L)Fe^{II}\cdots Cu^{II}(Cl)]^{+}$ ($\mathbf{3^{CuCl}}$) is assumed based on similarities to **4** and is therefore most similar in structure to $^{\mathbf{pmea}}\mathbf{2'\text{-}Cl}$. Such large structural differences amongst the various mononuclear copper(II)–chloride species ($^{\mathbf{R}}\mathbf{2'\text{-}Cl}$) may influence the electron-/atom-transfer ($Cl^{\bullet}$) chemistry, *vide infra*.

3.4. Spectroscopic characterization of the electron-/atom-($Cl^{\bullet}$) transfer reactions

3.4.1. UV–Vis spectroscopy

Iron porphyrinates have distinctive spectroscopic UV–Vis signatures, which dominate the charge transfer and/or d–d absorptions of copper(I) and/or copper(II) complexes. In CH_3CN at 298 K, $(F_8)Fe^{III}(Cl)$ ($\mathbf{1'\text{-}Cl}$) possesses a distinctive ligand-to-metal charge transfer (LMCT) band at 380 nm [30] along with π–π^{*} features observed within the Soret region at 414 nm and three less intense absorbances in the α-region at 504, 573, and 620 nm [17], Fig. 2. Addition of $[Cu^{I}(tmpa)(CH_3CN)]^{+}$ ($^{\mathbf{tmpa}}\mathbf{2}$), $[Cu^{I}(pmea)]^{+}$ ($^{\mathbf{pmea}}\mathbf{2}$), or $[Cu^{I}(pmap)]^{+}$ ($^{\mathbf{pmap}}\mathbf{2}$) to $\mathbf{1'\text{-}Cl}$ in CH_3CN results in electron-/atom- ($Cl^{\bullet}$) transfer reactions leading to complete formation of $[LCu^{II}(Cl)]^{+}$ ($^{\mathbf{R}}\mathbf{2'\text{-}Cl}$) and $(F_8)Fe^{II}$ (**1**), Scheme 2, the latter of which has characteristic absorbances at 424 nm (Soret) and 525 nm (α) [17], Fig. 2. No evidence for a reaction was observed upon addition of $[Cu^{I}(tepa)]^{+}$ ($^{\mathbf{tepa}}\mathbf{2}$) to $\mathbf{1'\text{-}Cl}$ in CH_3CN (Scheme 2).

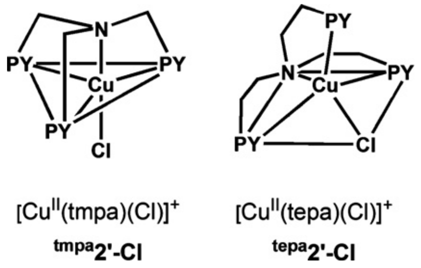

Complex	τ values
$^{\mathbf{tmpa}}\mathbf{2'\text{-}Cl}$	1.01
4	0.19
$^{\mathbf{pmea}}\mathbf{2'\text{-}Cl}$	0.12
$^{\mathbf{pmap}}\mathbf{2'\text{-}Cl}$	0.08
$^{\mathbf{tepa}}\mathbf{2'\text{-}Cl}$	0.01

Scheme 5.

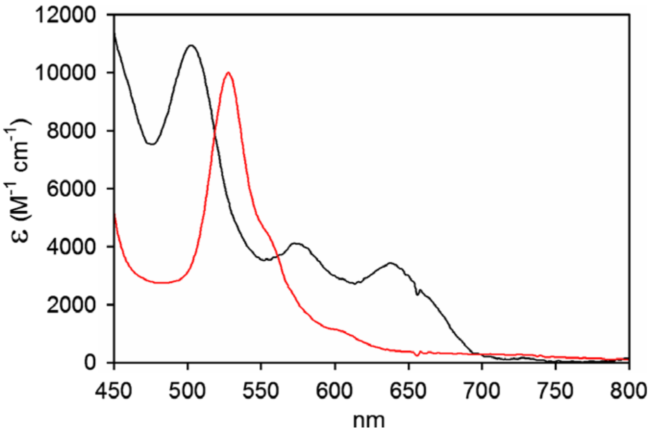

Fig. 2. UV–Vis spectra of the α-region for $(F_8)Fe^{III}(Cl)$ ($\mathbf{1'\text{-}Cl}$) in CH_3CN (black line) and the reduced $(F_8)Fe^{II}$ (**1**) complex upon addition of $[(L)Cu^{I}]^{+}$ to $\mathbf{1'\text{-}Cl}$ in CH_3CN (red line); where L is TMPA, PMEA, PMAP.

Dissolution of the heterobinucleating system, $[(^{6}L)Fe\cdots(Cl)\cdots Cu]^{+}$ (**3**) does not appear to result in $Cl^{\bullet}$ transfer from heme chemistry in CH_3CN at 298 K, as indicated by the α-region possessing the three bands typical of the ferric chloride species, Fig. 3. However, at lower concentrations of **3**, the UV–Vis features (π–π^{*}) broaden, the Soret absorbance shifts to lower energy (420 nm), and the LMCT band (380 nm) decreases in intensity suggesting partial $Cl^{\bullet}$ transfer from heme to copper, Fig. 4, i.e., there is an equilibrium mixture of $[(^{6}L)Fe^{III}(Cl)\cdots Cu^{I}]^{+}$ ($\mathbf{3^{FeCl}}$) and $[(^{6}L)Fe^{II}\cdots Cu^{II}(Cl)]^{+}$ ($\mathbf{3^{CuCl}}$), Scheme 3, also see further discussion below.

Nitrile solvents such as CH_3CN strongly coordinate to Cu^{I} and can even inhibit Cu^{I}/O_2 chemistry, as has been observed in tridentate ligand–copper/heme systems possessing similar pyridyl-ethyl-amine donor moieties [14,31].

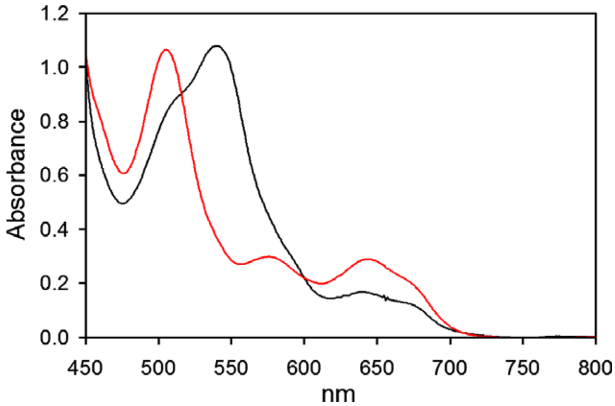

Fig. 3. UV–Vis spectra of the α-region indicate the presence of the $[(^{6}L)Fe^{III}(Cl)\cdots Cu^{I}]^{+}$:$[(^{6}L)Fe^{II}\cdots Cu^{II}(Cl)]^{+}$ ($\mathbf{3^{FeCl}}$):($\mathbf{3^{CuCl}}$) equilibrium in THF (black, clearly two peaks) and the predominantly $[(^{6}L)Fe^{III}(Cl)\cdots Cu^{I}]^{+}$ ($\mathbf{3^{FeCl}}$) equilibrium species in CH_3CN (red) at room temperature.

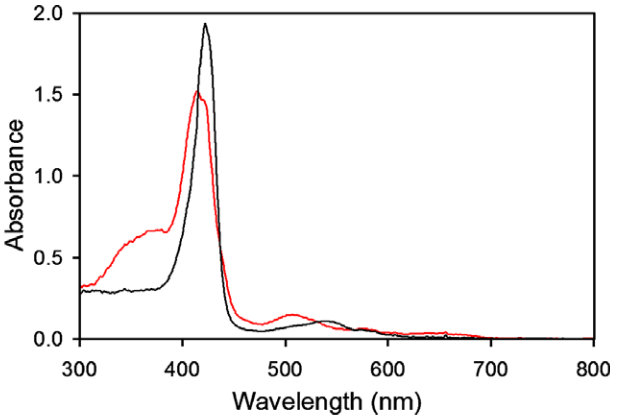

Fig. 4. UV–Vis spectra indicating the presence of the $[(^6L)Fe^{III}(Cl)\cdots Cu^I]^+$:$[(^6L)Fe^{II}\cdots Cu^{II}(Cl)]^+$ ($\mathbf{3^{FeCl}}$): ($\mathbf{3^{CuCl}}$) equilibrium in THF (black) and the predominantly $[(^6L)Fe^{III}(Cl)\cdots Cu^I]^+$ ($\mathbf{3^{FeCl}}$) in CH_3CN (red) at room temperature.

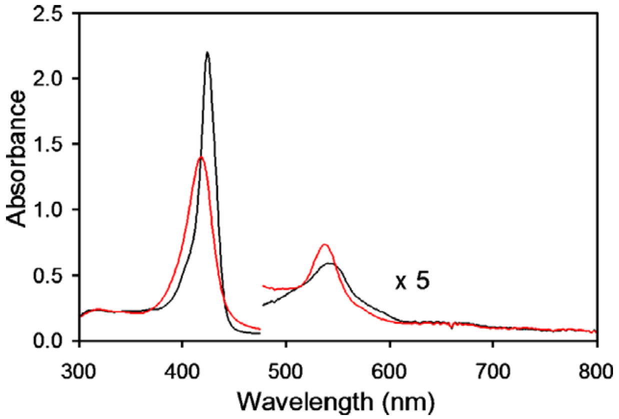

Fig. 5. UV–Vis spectra at 233 K in THF of $[(^6L)Fe^{II}\cdots Cu^{II}(Cl)]^+$ ($\mathbf{3^{CuCl}}$) (in black) and $[(^6L)Fe^{III}(O_2^-)\cdots Cu^{II}(Cl)]^+$ (in red).

Therefore, Cl$^\bullet$ transfer within **3** to copper is most likely hindered by CH_3CN solvent coordination to the Cu^I ion, see Scheme 6a. In an attempt to make the Cu^I ion of $[(^6L)Fe^{III}(Cl)\cdots Cu^I]^+$ ($\mathbf{3^{FeCl}}$) more accessible for efficient electron-/atom-transfer, the experiments were repeated in THF as solvent. However, in THF at all concentrations, there is a mixture of $[(^6L)Fe^{III}(Cl)\cdots Cu^I]^+$ ($\mathbf{3^{FeCl}}$) and $[(^6L)Fe^{II}\cdots Cu^{II}(Cl)]^+$ ($\mathbf{3^{CuCl}}$), as indicated by the broad absorbances observed in the Soret and α-region, Figs. 3 and 4. In contrast to the weak non-existent coordination of THF to Cu^I ions, ferrous hemes bind THF to form more stable complexes [8,17]. Therefore, such inefficient Cl$^\bullet$ transfer may be due to stabilization of the ferric chloride moiety by coordination of an axial base (THF), see Scheme 6b.

By decreasing the temperature of the solution of **3** to 233 K in either CH_3CN and THF at low complex concentration, the equilibrium shifts towards $[(^6L)Fe^{II}\cdots Cu^{II}(Cl)]^+$ ($\mathbf{3^{CuCl}}$), as confirmed by the sharpening of the Soret- and α-absorbances as well as the decrease in LMCT intensity (Fig. 5). Interestingly, upon addition of dioxygen, a stable superoxide species $[(^6L)Fe^{III}(O_2^-)\cdots Cu^{II}(Cl)]^+$ is generated in both CH_3CN and THF, Soret = 414 nm, α = 538 nm (Scheme 6c and Fig. 5). In the absence of chloride ligand, the reaction product of $[(^6L)Fe^{II}\cdots Cu^I]^+$ and dioxygen is established as a bridging peroxo species, $[(^6L)Fe^{III}(O_2^{2-})Cu^{II}]^+$ [3]. Here, in the absence of an electron from copper(I) to further reduce dioxygen to a peroxo species, we observe a stable heme-superoxide species; the UV–Vis absorptions are very characteristic and the same

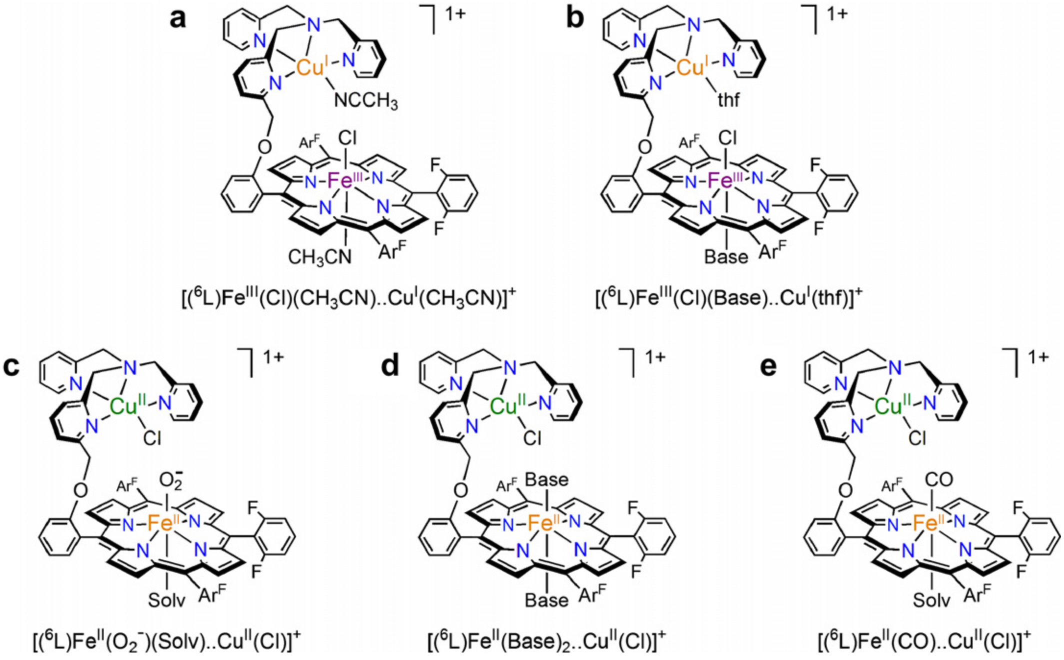

Scheme 6.

heme-superoxo formation chemistry has been established for reaction of O_2 with $(F_8)Fe^{II}$ and $(^6L)Fe^{II}$ (without Cu^I ion in tethered moiety) which form $[(F_8)Fe^{III}(O_2^-)]^+$ and $[(^6L)Fe^{III}(O_2^-)]^+$, respectively [17,32–34].

3.4.2. ^1H NMR spectroscopy

Multiple spin-state configurations are available for Fe^{II}/Fe^{III} coordination compounds leading to differences in reactivity amongst species of the same redox state. In CD_3CN at room temperature, the ^1H NMR spectrum of $(F_8)Fe^{III}(Cl)$ (**1′-Cl**) confirms a high spin $3d^5$ species as indicated by the paramagnetically shifted peak at δ 80 ppm for the pyrrole hydrogens [17]. Upon addition of $[Cu^I(tmpa)(CH_3CN)]^+$ ($^{\mathbf{tmpa}}\mathbf{2}$), $[Cu^I(pmea)]^+$ ($^{\mathbf{pmea}}\mathbf{2}$), or $[Cu^I(pmap)]^+$ ($^{\mathbf{pmap}}\mathbf{2}$), the pyrrole-H resonances are shifted upfield to δ 25 ppm (Fig. 6), representative of an equilibrium mixture of high- and low-spin $(F_8)Fe^{II}$ (**1**), Fig. 6. In previous work, the magnetic moment of **1** was determined at variable temperature via the Evans NMR method ($\mu = 4.1$) [17]. Upon lowering the temperature to 233 K, the pyrrole hydrogens displayed anti-Curie behavior, shifting upfield to δ 10 ppm in CH_3CN, indicative of full formation of low-spin six-coordinate heme (two axially bound CH_3CN such as in Scheme 6d) [17]. The absence of the ferric pyrrole-H resonances at δ 80 ppm upon adding $[LCu^I]^+$ ($^{\mathbf{R}}\mathbf{2}$) to **1′-Cl** suggests that electron-/atom-transfer is not affected by the spin state of the ferrous reaction product and that full conversion occurs, i.e., $Cl^{\bullet}$ transfer, forming $[LCu^{II}(Cl)]^+$ ($^{\mathbf{R}}\mathbf{2'}$**-Cl**) and $(F_8)Fe^{II}$ (**1**), Scheme 2.

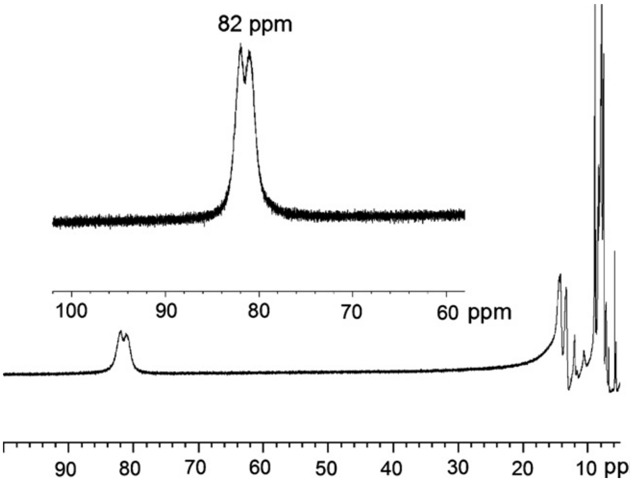

Fig. 7. ^1H NMR spectrum of $[(^6L)Fe^{III}(Cl)\cdots Cu^I]^+$ ($\mathbf{3^{FeCl}}$) in CD_3CN. The downfield paramagnetically shifted resonances centered at $\delta_{pyrrole} = 82$ ppm are consistent with the presence of only the high spin ferric chloride porphyrin complex.

The ^1H NMR spectrum of $[(^6L)Fe\cdots Cl\cdots Cu]^+$ (**3**) in CD_3CN (Fig. 7) looks nearly identical to the empty tether complex, $(^6L)Fe^{III}(Cl)$, suggesting that the $Cl^{\bullet}$ remains on the heme, i.e., no electron-/atom-transfer has taken place, as supported by UV–Vis spectroscopic analysis (*vide supra*). When changing to the more coordinating solvent for hemes, THF-d_8, we observe a mixture of Fe^{II} and Fe^{III} high spin species as revealed by the $[(^6L)Fe^{III}(Cl)\cdots Cu^I]^+$ ($\mathbf{3^{FeCl}}$) pyrrole peak at δ 80 ppm and the pyrrole resonances representative of $[(^6L)Fe^{II}\cdots Cu^{II}(Cl)]^+$ ($\mathbf{3^{CuCl}}$) at 50–55 ppm. Integration of the broad pyrrole resonances results in a roughly 1:1 mixture of the two species. Upon introduction of 1,5-dicyclohexylimidazole (DCHIm), a strongly coordinating axial base for heme, the equilibrium is pushed towards the $[(^6L)Fe^{II}\cdots Cu^{II}(Cl)]^+$ ($\mathbf{3^{CuCl}}$) conformer. Similarly, repeating the experiment in more strongly coordinating solvent, pyridine-d_5, results in a shift in equilibrium towards $[(^6L)Fe^{II}\cdots Cu^{II}(Cl)]^+$ ($\mathbf{3^{CuCl}}$), as observed by the presence of a pyrrole signal at δ 8.8 ppm, consistent with a low-spin ferrous species $[(^6L)Fe^{II}(py)_2\cdots Cu^{II}(Cl)]^+$ like that previous observed for $[(F_8)Fe^{II}(py)_2]$, Fig. 8 [17]. Therefore, the presence of an organic base like THF,

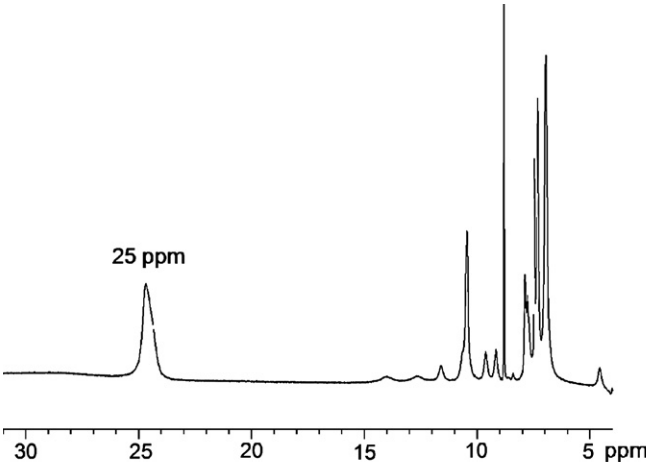

Fig. 6. ^1H NMR spectrum following the reaction of $(F_8)Fe^{III}(Cl)$ (**1′-Cl**) with $[Cu^I(tmpa)(CH_3CN)]^+$ ($^{\mathbf{tmpa}}\mathbf{2}$) in CD_3CN, δ (pyrrole) = 25 ppm. The product is a mixture of high (with one ligated axial CD_3CN) and low-spin (two ligated axial CD_3CN molecules) $(F_8)Fe^{II}$ (**1**) plus $[Cu^{II}(tmpa)(Cl)]^+$ ($^{\mathbf{tmpa}}\mathbf{2'}$**-Cl**).

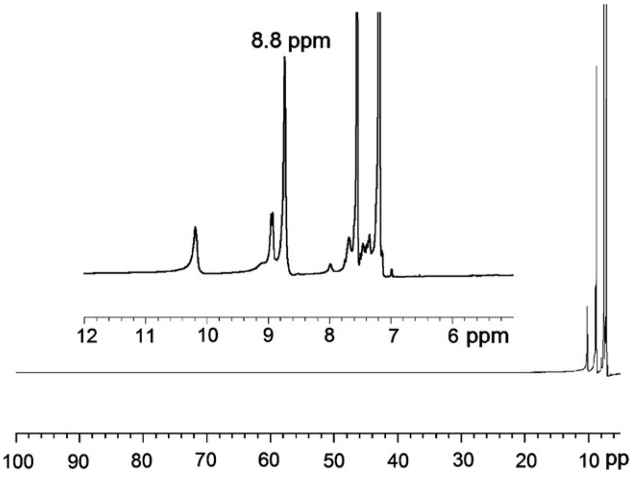

Fig. 8. ^1H NMR spectrum of $[(^6L)Fe^{II}\cdots Cu^{II}(Cl)]^+$ ($\mathbf{3^{CuCl}}$) in pyridine-d_5. No paramagnetic resonances were observed as the coordinating ability of pyridine forces the equilibrium to the low-spin d_6 ferrous porphyrin complex. $\delta_{pyrrole} = 8.8$ ppm.

DCHIm, or pyridine-d_5 will clearly push the equilibrium (Scheme 3) entirely to the stabilized low-spin d_6 ferrous state to form $[(^6L)Fe^{II}(Base)_2\cdots Cu^{II}(Cl)]^+$ (Scheme 6d). The sensitive nature of this reaction in non-coordinating solvents suggests that the redox potentials of the two metal centers are nearly identical under such conditions. This supposition is substantiated by the electrochemical studies, see below.

3.4.3. Electron paramagnetic resonance (EPR) spectroscopy

X-band EPR analyses were conducted on frozen samples (12–16 K; 1–2 mM) in CH_3CN:toluene (1:1) solvent mixtures. $(F_8)Fe^{III}(Cl)$ (**1′-Cl**) has a typical high spin $3d^5$ heme signal with $g_\perp = 5.92$ and $g_\parallel = 2.00$, Fig. 9. Upon addition of DCHIm, the signal changes to a low-spin $3d^5$ species due to coordination of a strong axial base to the heme, forming $(F_8)Fe^{III}(Cl)(DCHIm)$. Instead, addition of 1 equiv. of $[Cu^I(tmpa)(CH_3CN)]^+$ (**^{tmpa}2**) to **1′-Cl** results in complete silencing of the heme species indicative of the formation of an Fe^{II} $3d^6$ system and the presence of a reverse axial signal ($g_\perp = 2.01$, $g_\parallel = 2.18$, $A_\perp = 96\,cm^{-1}$) typical of a trigonal bipyramidal Cu^{II} $3d^9$ system, as previously established for **^{tmpa}2′-Cl** (Fig. 9) [28,35]. The complete silencing of the iron is consistent with a quantitative efficient electron-/atom-transfer ($Cl^\bullet$) process, Scheme 2.

As expected, the EPR spectrum of binuclear $[(^6L)Fe\cdots Cl\cdots Cu]^+$ (**3**) upon dissolution in an CH_3CN:toluene (1:1) solvent mixture displays only high spin ferric chloride; cuprous ion is EPR silent, Fig. 10. Addition of DCHIm, results in complete silencing of the ferric EPR signal and appearance of an axial signal ($g \sim 2$) due to the presence of a copper(II) species, Fig. 10. As opposed to the mononuclear F_8 system versus the ^6L system, a low-spin $3d^5$ iron(III) species is not observed upon addition of a coordinating base, implying formation of $[(^6L)Fe^{II}(DCHIm)_2\cdots Cu^{II}(Cl)]^+$, Scheme 6d. The poorly resolved axial (but not "reverse") EPR signal is due to the $[(L)Cu^{II}(Cl)]^+$ moiety, distorted from tbp because of the pyridyl 6′-substituent in accordance with previous studies [29].

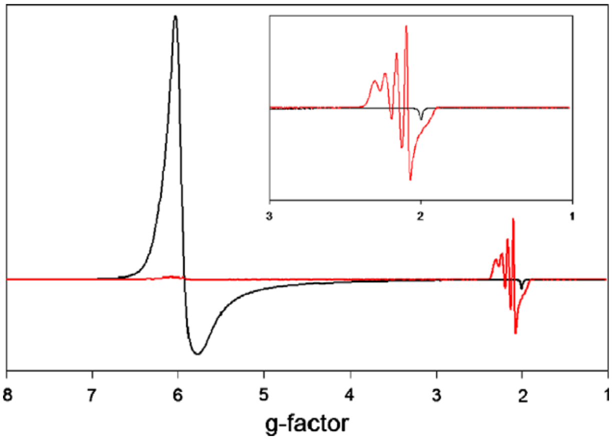

Fig. 9. X-band EPR spectra of ($T = 12$–16 K) of $(F_8)Fe^{III}(Cl)$ (**1′-Cl**) (black) and the product mixture of **1′-Cl** and $[Cu^I(tmpa)(CH_3CN)]^+$ (**^{tmpa}2**) (red).

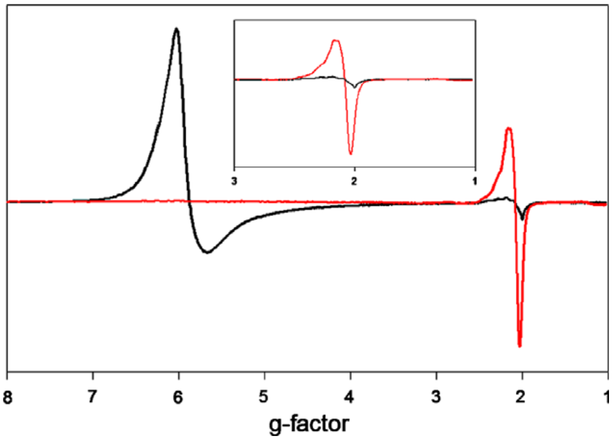

Fig. 10. X-band EPR spectra of $[(^6L)Fe\cdots Cl\cdots Cu]^+$ (**3**) (black) and $[(^6L)Fe^{II}(DCHIm)_2\cdots Cu^{II}(Cl)]^+$ (Scheme 6d) (red).

3.4.4. Infrared spectroscopy

Since $[(^6L)Fe^{II}(Base)_{1-2}\cdots Cu^{II}(Cl)]^+$ is favored in the presence of an axial base (i.e., DCHIm, THF, and pyridine-d_5), IR spectroscopy was employed to further confirm complete $Cl^\bullet$ transfer by addition of CO to $[(^6L)Fe\cdots Cl\cdots Cu]^+$ (**3**). CO binds to both iron and copper ions in the reduced state [7]; therefore the location of the coordinated chlorine can be assumed based on the carbonyl species formed. Previously, the bis-carbonyl complex $[(^6L)Fe^{II}(CO)\cdots Cu^I(CO)]^+$ was characterized with $\nu_{CO}(Fe) = 1975\,cm^{-1}$ and $\nu_{CO}(Cu) = 2091\,cm^{-1}$ [7]. Upon addition of CO to **3** in CH_3CN, only $\nu_{CO}(Fe) = 1975\,cm^{-1}$ is observed, indicating formation of $[(^6L)Fe(CO)\cdots Cu(Cl)]^+$ (**5**) (Scheme 6e) and confirming that the equilibrium shifts towards the ferrous state with bound CO.

3.5. Electrochemical estimates of the driving force (ΔG°) for the electron-/atom- ($Cl^\bullet$) transfer reactions

Heme species can involve many redox changes, over a number of oxidation states, i.e., IV/III, III/II, and II/I [24,36–38]. In addition, the porphyrin ring can be oxidized or reduced to a cation or anion radical [24]. To describe electron-/atom-transfer chemistry in the present systems, Fe^{III}/Fe^{II} and Cu^{II}/Cu^I redox processes are of primary concern. Cyclic voltammetric measurements were carried out on CH_3CN solutions of each complex under investigation; $E_{1/2}$ values are reported in Tables 1 and 2. All voltammograms were classified as quasi-reversible having $i_{pc}/i_{pa} \approx 1$ with half-wave potentials in the range $E_{1/2} = +60$ to -740 mV versus Fc/Fc^+ with $\Delta E = 60$–300 mV.

In the present study, the redox potentials ($E_{1/2}$) of the mononuclear cupric chloride species (**^{R}2′-Cl**) and $(F_8)Fe^{II}$ (**1**) were determined *in situ* upon dissolution of the complementary cuprous salt (**^{R}2**) in an CH_3CN solution containing 1 equiv. of $(F_8)Fe^{III}(Cl)$ (**1′-Cl**), (Scheme 2) and

Table 1
Redox potentials recorded in CH_3CN at room temperature of various synthetic hemes and copper complexes

Complex	$E_{1/2}$ (mV vs. Fc/Fc^+)	ΔE (mV)	Redox couple
$[Cu^I(tmpa)(CH_3CN)]^+$ (**^{tmpa}2**)	−400	100	$Cu^{II/I}$
$[Cu^{II}(tmpa)(Cl)]^+$ (**^{tmpa}2′-Cl**)	−740	130	$Cu^{II/I}$
$[Cu^I(pmea)]^+$ (**^{pmea}2**)	−360	300	$Cu^{II/I}$
$[Cu^{II}(pmea)(Cl)]^+$ (**^{pmea}2′-Cl**)	−670	130	$Cu^{II/I}$
$[Cu^I(pmap)]^+$ (**^{pmap}2**)	−250	300	$Cu^{II/I}$
$[Cu^{II}(pmap)(Cl)]^+$ (**^{pmap}2′-Cl**)	−590	110	$Cu^{II/I}$
$[Cu^I(tepa)]^+$ (**^{tepa}2**)	60	100	$Cu^{II/I}$
$[(F_8TPP)Fe^{II}]$ (**1**)	−140	100	$Fe^{III/II}$
$[(F_8TPP)Fe^{III}(Cl)]$ (**1′-Cl**)	−530	80	$Fe^{III/II}$

See text for references to previously measured values.

Table 2
Half-wave potentials measured in CH_3CN at room temperature for $[(^6L)Fe\cdots Cl\cdots Cu]^+$ (**3**) and derivatives[a]

Complex	$E_{1/2}$ (mV vs. Fc/Fc^+)	ΔE (mV)	Redox couple
$(^6L)Fe^{II}$	−170	100	$Fe^{III/II}$
$(^6L)Fe^{III}(Cl)$	−560	100	$Fe^{III/II}$
$[(^6L)Fe\cdots(Cl)\cdots Cu^I]^+$ (**3**)	−530	110	$Fe^{III/II}$, $Cu^{II/I}$
$[(^6L)Fe^{II}(DCHIm)_2\cdots Cu^{II}(Cl)]$	−490	60	$Fe^{III/II}$
$[(^6L)Fe^{II}(DCHIm)_2\cdots Cu^{II}(Cl)]$[b]	−650	110	$Cu^{II/I}$

[a] All measurements were made under 1 atm of argon unless stated otherwise.

[b] Measured under 1 atm of carbon monoxide.

(100 mM) tetrabutylammonium hexafluorophosphate electrolyte. Since electron-/atom-transfer does not occur upon mixing **^{tepa}2** and $(F_8)Fe^{III}(Cl)$, the $E_{1/2}$ value of $[Cu^{II}(tepa)(Cl)]B(C_6F_5)_4$ in CH_3CN was not determined here but it is known to be nearly 0.5 V more positive than that for **^{tmpa}2′-Cl** [12].

The $E_{1/2}$ values for the $[B(C_6F_5)_4]^-$ salts of the various cuprous and cupric chloride species followed the same trend as was previously obtained for their $[LCu^I]PF_6$ and $[LCu^{II}(Cl)]ClO_4$ analogues in dimethylformamide (DMF) [11,39]. Upon increasing the chelate ring size (i.e., ligand arm length) of the ligands housing the copper ion, the $E_{1/2}$ values become more positive, favoring copper(I), see Fig. 11 and Table 1. The most positive redox potential, $E_{1/2} = +60$ mV, assigned to $[Cu^I(tepa)]^+$ (**^{tepa}2**), is explained by the near-ideal tetrahedral ligand framework provided by TEPA which is the most stable geometry for a cuprous species.

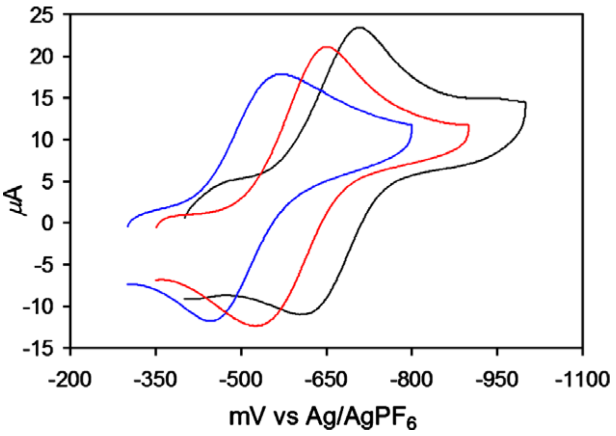

Fig. 11. Cyclic voltammograms of $[Cu^{II}(tmpa)(Cl)]^+$ (**^{tmpa}2′-Cl**) (black), $[Cu^{II}(pmea)(Cl)]^+$ (**^{pmea}2′-Cl**) (red), and $[Cu^{II}(pmap)(Cl)]^+$ (**^{pmap}2′-Cl**) (blue) in CH_3CN with $(Bu)_4NPF_6$ referenced against $Ag/AgPF_6$. Each complex was generated *in situ* from the addition of $(F_8)Fe^{III}(Cl)$ (**1′-Cl**) to $[(L)Cu^I]B(C_6F_5)_4$ (**^{R}2**). The redox wave for the reduced $(F_8)Fe^{II}$ (**1**) complex occurs at −140 mV (not shown/off-scale) vs. Fc^+/Fc.

Chloride, a strongly coordinating anion, stabilizes the more highly charged metal ion species, resulting in a negative shift of the Cu^{II}/Cu^I and Fe^{III}/Fe^{II} redox potentials. The $E_{1/2}$ values of the cupric chloride species are ~300 mV more negative than their cuprous partner species, this value being conserved for each copper species, Table 1. Such trends in $E_{1/2}$ values for $[LCu^{II}(Cl)]^+$ (**^{R}2′-Cl**) and their corresponding $[LCu^I]^+$ (**^{R}2**) compounds are within the same range and parallel to those from an analogous study on quinolyl-for-pyridyl systematic ligand variations [39]. Moreover, the $E_{1/2}$ value of **1** shifts from −140 mV to −530 mV for **1′-Cl** in CH_3CN, Table 1.

From the redox potentials obtained for the heme and copper complexes, the relative driving force ($\Delta G°$) for the overall electron-/atom- ($Cl^•$) transfer process was estimated by calculating [$E_{1/2}$(oxidant) − $E_{1/2}$(reductant)]. The driving force was found through systematic variation of $E_{1/2}$(reductant) as a function of the ligand environment around copper. The ferric oxidant **1′-Cl** reacts with all of the $[(L)Cu^I]^+$ complexes discussed here, Scheme 2, with the exception of $[Cu^I(tepa)]^+$ (**^{tepa}2**). The overall negative driving force for the reaction with **^{tepa}2** ($\Delta E° = -200$ mV) indicates that a reaction should not occur which is consistent with the UV–Vis results (*vide infra*). In addition, we find **1′-Cl** should oxidize **^{tmpa}2** the most effectively, with a driving force of $\Delta E^{\circ} = +210$ mV while the $^{\mathbf{pmap}}\mathbf{2}$ reaction with **1′-Cl** should be the least effective, having a much smaller driving force, $\Delta E^{\circ} = +60$ mV. When calculating the driving force values, we were consistent in using those $E_{1/2}$ values determined in the presence of a chloride anion as this has shown to significantly influence the $Fe^{III/II}$ and $Cu^{II/I}$ reduction potentials.

Consistent with the −390 mV difference in the reduction potential of $(F_8)Fe^{III/II}(Cl)$ and $(F_8)Fe^{III/II}$, the $E_{1/2}$ value for $(^6L)Fe^{III/II}(Cl)$ shifts from −560 mV to −170 mV for $(^6L)Fe^{III/II}$. Surprisingly, only a small change in the overall redox potential ($E_{1/2} = -530$ mV) occurs upon addition of a cuprous salt into the non-heme tethered portion of $(^6L)Fe^{III}(Cl)$ to form $[(^6L)Fe\cdots Cl\cdots Cu]$ (**3**), Fig. 12. The visual presence of only one reversible wave suggests that the redox waves observed in cyclic voltammetry corresponding to the $Fe^{III/II}$ and $Cu^{II/I}$ potentials are overlapping (if not identical). Similarly, overlapping heme/M (M = Cu, non-heme iron) redox processes have been observed [40–42]. By considering the Nernst equation, if $E_{1/2}(Cu) = E_{1/2}(Fe)$ then $K \approx 1$, an equilibrium state (Scheme 3) is suggested and ∼1:1 molar ratios of $[(^6L)Fe^{III}(Cl)\cdots Cu^I]^+$ ($\mathbf{3^{FeCl}}$) and $[(^6L)Fe^{II}\cdots Cu^{II}(Cl)]^+$ ($\mathbf{3^{CuCl}}$) are present, as supported by ^1H NMR spectroscopy (*vide infra*).

The $Fe^{III/II}$ and $Cu^{II/I}$ redox waves for $[(^6L)Fe\cdots Cl\cdots Cu]^+$ (**3**) separate in the presence of external substrates (i.e., CO and DCHIm), Fig. 12 and Table 2. More specifically, addition of DCHIm to **3** results in the $Cu^{II/I}$ redox potential shifting negative to $E_{1/2} = -650$ mV and a positive shift of the $Fe^{III/II}$ redox potential to $E_{1/2} = -490$ mV occurs. Following ^1H NMR and EPR spectral analysis, a low-spin $[(^6L)Fe^{II}(DCHIM)_2\cdots Cu^{II}(Cl)]^+$ species is the likely reaction product. Upon addition of CO to this solution, the $Fe^{III/II}$ redox potential is rendered irreversible yet the $Cu^{II/I}$ redox potential does not change, Table 2. In the case of $[(^6L)Fe\cdots Cl\cdots Cu]$ (**3**), it is interesting to find that upon addition of Lewis bases known to stabilize ferrous hemes that the redox waves also separate, meaning the $E_{1/2}$ values of the two metal ions are no longer equivalent and the equilibrium lies towards $\mathbf{3^{CuCl}}$.

3.6. Observed rates of electron-/atom- ($Cl^{\bullet}$) transfer as determined by stopped-flow UV–Vis spectroscopy

Using a stopped-flow kinetics instrument with UV–Vis spectroscopic monitoring, equimolar THF solutions of $[(L)Cu^I]^+$ ($^{\mathbf{R}}\mathbf{2}$) and $(F_8)Fe^{III}(Cl)$ (**1′-Cl**) complexes were rapidly mixed at variable low temperatures (188–263 K) in order to gain further insight into the electron-/atom- ($Cl^{\bullet}$) transfer process, Scheme 2. As discussed, the calculated relative driving forces predicted relative rates corresponding to the measured redox potentials of the various cuprous reductants in the order $[Cu^I(tmpa)(CH_3CN)]^+$ ($^{\mathbf{tmpa}}\mathbf{2}$) > $[Cu^I(pmea)]^+$ ($^{\mathbf{pmea}}\mathbf{2}$) > $[Cu^I(pmap)]^+$ ($^{\mathbf{pmap}}\mathbf{2}$). In contrast, we find the relative rates to be $^{\mathbf{pmea}}\mathbf{2} \gg {}^{\mathbf{pmap}}\mathbf{2} > {}^{\mathbf{tmpa}}\mathbf{2}$, determined qualitatively. In fact, the reduction of **1′-Cl** by $^{\mathbf{pmea}}\mathbf{2}$ in THF is too fast to be monitored by stopped-flow kinetics even at 188 K whereas the reaction involving $^{\mathbf{tmpa}}\mathbf{2}$ (Figs. 13 and 14) takes greater than 5 minutes to complete at 233 K. The reaction involving $^{\mathbf{pmap}}\mathbf{2}$ at 188 K is observed on a millisecond time-scale (Figs. 15 and 16). The kinetic traces that we monitor for reactions involving $^{\mathbf{tmpa}}\mathbf{2}$ at 233 K (Fig. 14) and $^{\mathbf{pmap}}\mathbf{2}$ at 188 K (Fig. 16) both fit a first-order kinetic model, $k_{obs} = 1.42 \times 10^{-5}\ s^{-1}$ and $3 \times 10^{-2}\ s^{-1}$ respectively. These results are somewhat unexpected and for the purposes of the present study which emphasizes qualitative aspects of the present relatively uncommon electron-/atom- ($Cl^{\bullet}$) transfer chemistry, further kinetic studies have not been pursued. Future efforts will include studies involving solvent and metal complex

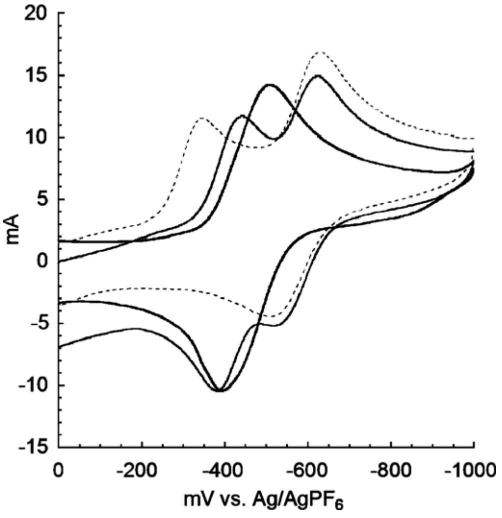

Fig. 12. Cyclic voltammograms recorded in CH_3CN with $(Bu)_4NPF_6$ as the supporting electrolyte of $[(^6L)Fe\cdots Cl\cdots Cu]^+$ (**3**) (black), $[(^6L)Fe^{II}(DCHIm)_2\cdots Cu^{II}(Cl)]$ (Scheme 6d) (gray), and $[(^6L)Fe^{II}(DCHIm)_2\cdots Cu^{II}(Cl)] + CO$ (dashed line).

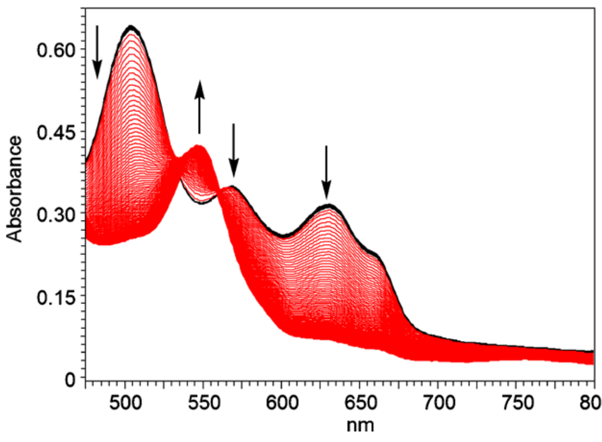

Fig. 13. Time-dependent UV–Vis spectra (time = 0–375 s) for the $Cl^{\bullet}$ transfer reaction of $(F_8)Fe^{III}(Cl)$ (**1′-Cl**) to $[Cu^I(tmpa)(THF)]^+$ ($^{\mathbf{tmpa}}\mathbf{2}$) in THF at 233 K.

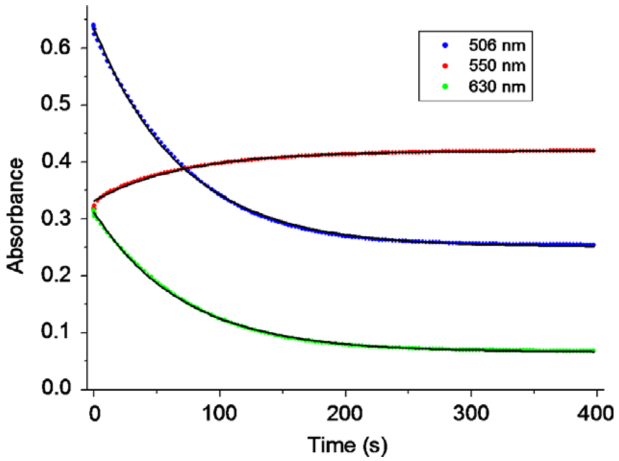

Fig. 14. Absorption changes as a function of time from stopped-flow UV–Vis spectroscopy measured at 506 nm (blue), 550 nm (red), and 630 nm (green) following the reaction of $(F_8)Fe^{III}(Cl)$ (**1′-Cl**) and $[Cu^{I}(tmpa)(THF)]^{+}$ (**^{tmpa}2**) in THF at 233 K. First order kinetic fits are overlaid as black lines, $k_{obs} = 1.42 \times 10^{-5}\ s^{-1}$.

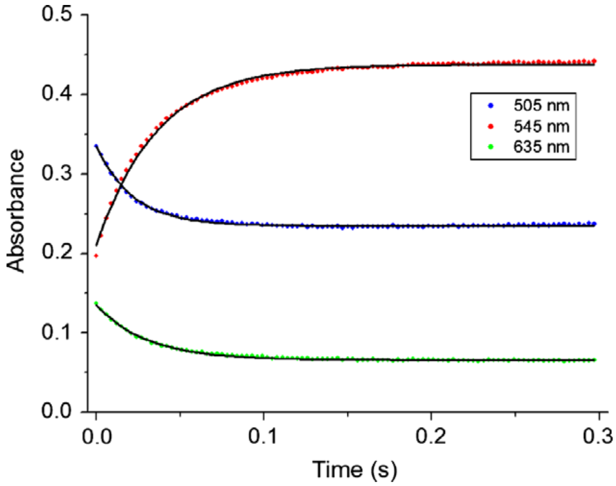

Fig. 16. Absorption changes as a function of time from stopped-flow UV–Vis spectroscopy measured at 505 nm (blue), 545 nm (red), and 630 nm (green) following the reaction of $(F_8)Fe^{III}(Cl)$ (**1′-Cl**) and $[Cu^{I}(pmap)]^{+}$ (**^{pmap}2**) in THF at 188 K. First order kinetic fits are overlaid as black lines, $k_{obs} = 3 \times 10^{-2}\ s^{-1}$.

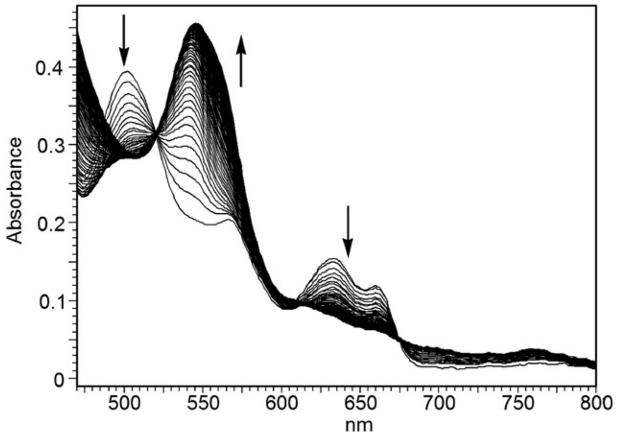

Fig. 15. Time-dependent UV–Vis spectra (time = 0–300 ms) for the $Cl^{\bullet}$ transfer reaction of $(F_8)Fe^{III}(Cl)$ (**1′-Cl**) to $[Cu^{I}(pmap)]^{+}$ (**^{pmap}2**) in THF at 188 K.

concentration variations, to elucidate further mechanistic aspects.

3.7. Likely inner-sphere electron-/atom- ($Cl^{\bullet}$) transfer chemistry

While the rates for $Cl^{\bullet}$ transfer varied over impressive ranges, from too fast for stopped-flow kinetics to milliseconds to minutes, by tuning the copper ligand environment, there was no correlation with the thermodynamic driving force estimated from cyclic voltammetry measurements. Such correlations are well known for outer-sphere electron-transfer processes both experimentally [43,44] and theoretically [45]. Therefore, the lack of a free energy correlation suggests that there are indeed important contributions to the rates from "inner-sphere" pathways like those first described by Taube [46]. For an inner-sphere mechanism, the formation of a chlorine bridge between iron and copper (Scheme 7) precedes electron-/atom- ($Cl^{\bullet}$) transfer. As a result, the thermodynamics calculated (*vide supra*) from the free mononuclear compounds are not necessarily relevant. Other factors are expected to play important roles, such as those arising from bond breakage and formation and variations in electronic coupling across the halide bridge [47–49].

The chemical nature of this putative halide bridged inner-sphere complex remains speculative as no intermediates were observed during the course of the reactions. The structural changes associated with bridge formation about copper are expected to be more significant than that at the heme (*vide supra*). In this regard it is interesting to note that the rates were fastest for **^{pmea}2** and slowest for **^{tmpa}2**. As described previously (Section 3.3), $Cl^{\bullet}$ transfer for the latter compound involves a change in coordination number, deligation of one of the pyridyl arms, and solvent coordination, Scheme 4. The latter two processes are absent for **^{pmea}2** (and **^{pmap}2**). Therefore, although it is speculative at this time, the results are consistent with expectations that geometric changes about copper are very important in determining the rates of $Cl^{\bullet}$ transfer.

3.8. Observed rates of electron-/atom- ($Cl^{\bullet}$) transfer and bimolecular rate constant for CO rebinding as determined by transient absorption spectroscopy

Due to the binucleating nature of ^{6}L, stopped-flow UV–Vis spectroscopy could not be utilized to measure the rates of electron-/atom- ($Cl^{\bullet}$) transfer. Instead, a complementary approach, transient absorption laser flash photolysis (TA), was employed. Here we took advantage of the well documented photodissociation of carbon monoxide from heme–carbonyl compounds. The photorelease of CO is

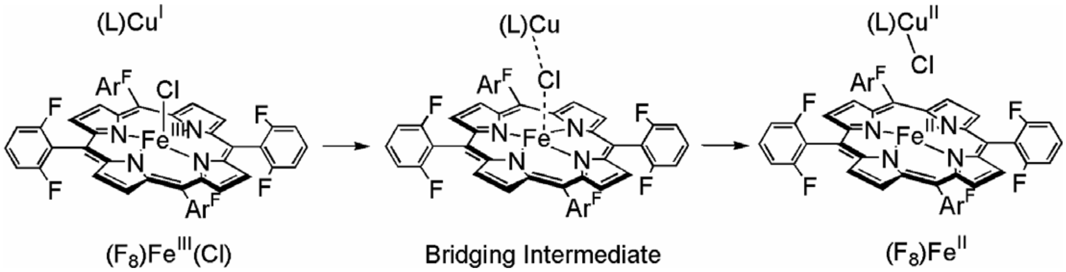

Scheme 7.

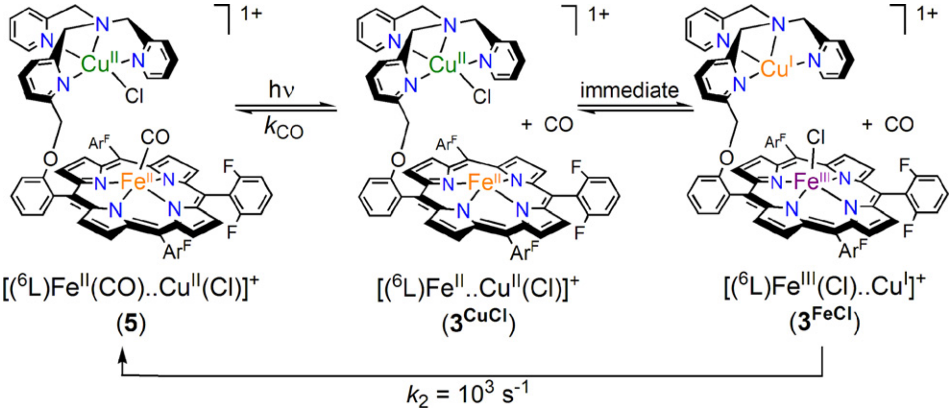

Scheme 8.

known to occur with a quantum yield of unity in both natural and synthetic hemes [50,51].

We therefore prepared the compound $[(^6L)Fe^{II}(CO)\cdots Cu^{II}(Cl)]^+$ (**5**) by dissolution of $[(^6L)Fe\cdots(Cl)\cdots Cu]^+$ (**3**) in CH_3CN and bubbling with CO(g), Scheme 6e. Upon excitation ($\lambda_{ex} = 532$ nm; 8–10 ns FWHM) of **5** with pulsed light in CH_3CN under 1 atm CO (Scheme 8), the photoinitiated ejection of CO occurs and the rate at which the initial species reforms could be measured. Typical absorption difference spectra for such an experiment are shown at the indicated delay times after the laser pulse in Fig. 17. It was apparent from both the appearance wavelength dependent bi-exponential kinetics, Eq. (1), that two different species were photogenerated within the time response of our apparatus (~10 ns). At wavelengths

$$A(t) = A_1 \exp(-k_1 t) + A_2 \exp(-k_2 t) \quad (1)$$

lower than 375 nm, the absorption transients were almost perfectly exponential as the second state did not absorb light appreciably at this wavelength. This allowed us to accurately determine the value of k_2. With this information, k_2 was fixed and the value of k_1 was determined at the wavelength with the highest signal-to-noise ratio, ~420 nm. With these two rate constants fixed, the wavelength dependent absorption changes were fit to Eq. (1) and only the amplitudes were allowed to vary. The amplitudes of A_1 and A_2 as a function of time are shown in Fig. 17a and 17b alone. We note that this is a standard kinetic analysis termed "decay associated spectra" by Brand and coworkers [52].

The time resolved spectra in Fig. 17a were obtained upon photodissociation of CO from $[(^6L)Fe^{II}(CO)\cdots Cu^{II}(Cl)]^+$ (**5**) and they correlate to formation of the bis-solvento species, $[(^6L)Fe^{II}(CH_3CN)_2\cdots Cu^{II}(Cl)]^+$ ($\mathbf{3^{CuCl}}$). Support for this assignment was gained by subtracting the absorption spectrum of **5** from $\mathbf{3^{CuCl}}$, Abs$[(^6L)Fe^{II}(CH_3CN)_2\cdots Cu^{II}(Cl)]^+$ ($\mathbf{3^{CuCl}}$) − Abs$[(^6L)Fe^{II}(CO)\cdots Cu^{II}(Cl)]^+$ (**5**), and overlaying the resulting spectrum on the transient data, Fig. 17a. The excellent agreement gives little doubt that this intermediate has been correctly assigned. In addition, we found that the lifetime of the solvent compound showed a first-order dependence on the CO concentration. A linear plot of k_1 (s^{-1}) versus [CO] yielded a bimolecular rate constant of $k_{CO} = 1.4 \times 10^7\ M^{-1}\ s^{-1}$, inset Fig. 17a. This value is in the same range as that measured for CO recombination to other synthetic and biological hemes.

As a source of further comparison, the bimolecular rate constant for CO rebinding to $(F_8)Fe^{II}$ (**1**) in CH_3CN upon photodissociation from $(F_8)Fe^{II}(CO)$ was also determined here as $k_{CO} = 6.0 \times 10^5\ M^{-1}\ s^{-1}$, Fig. 18. The greater than two orders of magnitude difference between k_{CO} for $[(^6L)Fe^{II}(CO)\cdots Cu^{II}(Cl^{\cdot})]^+$ (**5**) versus $(F_8)Fe^{II}(CO)$ shows that for **5**, the presence of the copper(II) moiety or the difference in heme structure (F_8 versus ^6L) has a large effect on the chemistry at the Fe^{II} ion in $[(^6L)Fe^{II}\cdots Cu^{II}(Cl)]^+$ ($\mathbf{3^{CuCl}}$) as concerns CO rebinding. One possible explanation

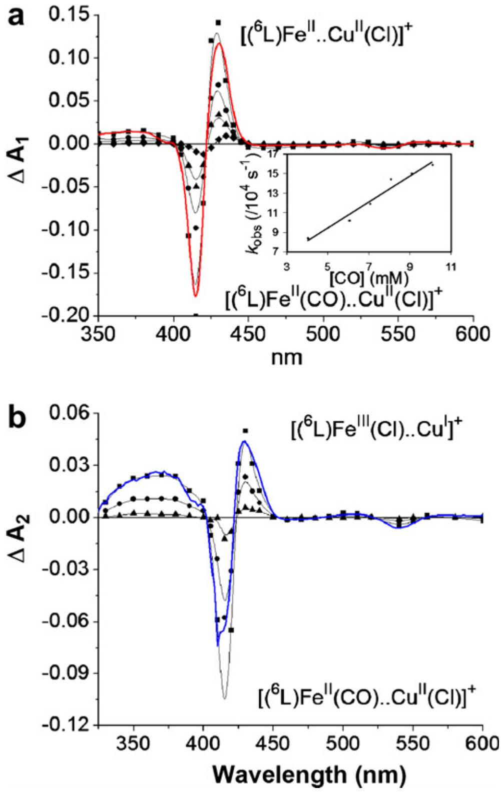

Fig. 17. Transient absorption difference spectra obtained after photolysis of $[(^6L)Fe^{II}(CO)\cdots Cu^{II}(Cl)]^+$ (**5**) in CO saturated CH_3CN yielding (a) $[(^6L)Fe^{II}\cdots Cu^{II}(Cl)]^+$ (**3^{CuCl}**) with various delay times monitored at 10 ns (squares), 5 μs (circles), 10 μs (triangles), and 30 μs (diamonds) where the red calculated difference spectrum {Abs$[(^6L)Fe^{II}\cdots Cu^{I}]^+$ – Abs$[(^6L)Fe^{II}(CO)\cdots Cu^{II}(Cl)]^+$ (**5**)} is displayed for comparison and the inset displays the CO dependence of this process where the slope yields, k_{CO} (298 K) = 1.4×10^7 M^{-1} s^{-1}, (b) $[(^6L)Fe^{III}(Cl)\cdots Cu^{I}]^+$ (**3^{FeCl}**) with various extrapolated delay times at 10 ns (squares), 30 μs (circles), and 60 μs (triangles) where the blue calculated difference spectrum {Abs$[(^6L)Fe^{III}(Cl)\cdots Cu^{I}]^+$ (**3^{FeCl}**) – Abs$[(^6L)Fe^{II}(CO)\cdots Cu^{II}(Cl)]^+$ (**5**)} is displayed for comparison.

is that ^6L is a better donor ligand to iron in comparison to F_8, due to the simple fact of having two less aryl fluoro-substituents on the heme. There exists literature precedent for this, i.e., increased rates for small molecule binding to the heme in a heterobinuclear complex compared to binding to $(F_8)Fe^{II}$. For example, we previously published the bimolecular recombination of CO to $[(^6L)Fe^{II}(thf)_2\cdots Cu^{I}(CO)]^+$ and $(F_8)Fe^{II}(thf)_2$ (**1**) following photolysis of $[(^6L)Fe^{II}(CO)\cdots Cu^{I}(CO)]^+$ and $(F_8)Fe^{II}(CO)$, yielding the second-order rate constants of 1.0×10^7 M^{-1} s^{-1} and 3.2×10^6 M^{-1} s^{-1} respectively [8]. Furthermore, a similar observation concerning rates was found upon reaction of O_2 with a related Fe/Cu system, $[(^2L)Fe^{II}\cdots Cu^{I}]^+$, in which the copper moiety of ^2L is tridentate in nature and comprised of a central amine with two pyridyl-ethyl-N-donors. In comparison to the intermolecular initial reaction of O_2 with the heme only $(F_8)Fe^{II}$ (forming a heme–O_2 adduct) in a $(F_8)Fe^{II}$/LCu^I mixture, the analogous intramolecular reaction involving the heterobinucleating ligand (^2L) to form $[(^2L)Fe^{III}(O_2^-)\cdots Cu^{I}]^+$ was more than 20 times faster [14].

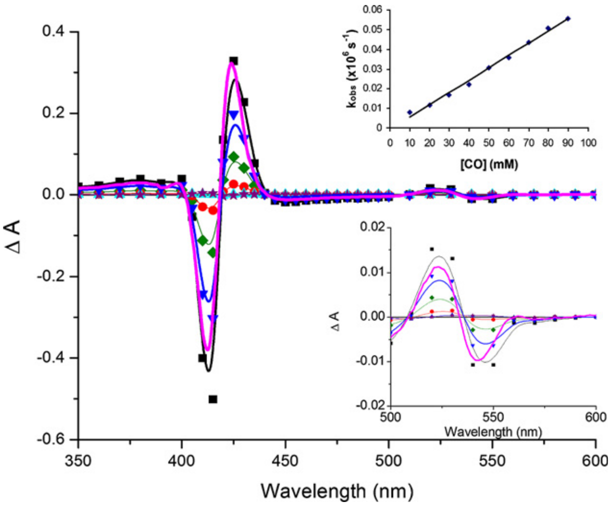

Fig. 18. Transient absorption difference spectra obtained after photolysis of $F_8Fe^{II}(CO)(CH_3CN)$ in CO saturated CH_3CN yielding $F_8Fe^{II}(CH_3CN)_2$ (**1**) with various delay times monitored at 0 μs (black squares), 10 μs (blue triangles), 25 μs (green diamonds), 50 μs (red circles), 100 μs (turquoise triangles) and 250 μs (purple stars) where the pink calculated difference spectrum {Abs$[F_8Fe^{II}(CH_3CN)_2]$ (**1**) – Abs$[F_8Fe^{II}(CO)(CH_3CN)]$} is displayed for comparison in the lower inset and the linear plot in the upper inset displays the CO dependence of this process where the slope yields, k_{CO} (298 K) = 6.0×10^5 M^{-1} s^{-1}.

The data for the other perhaps more interesting process that occurs after photodissociation of CO from $[(^6L)Fe^{II}(CO)\cdots Cu^{II}(Cl)]^+$ (**5**) is shown in Fig. 17b. The appearance of a new broad absorption band at ~375 nm is characteristic of an iron species in the Fe(III) formal oxidation state. Suslick has assigned this as a ligand-to-metal charge-transfer (LMCT) band and reported that the position of this band can be correlated with the donor ability of the axial ligand [30]. The experimental data observed here is indeed in excellent agreement with the calculated difference spectrum of Abs$[(^6L)Fe^{III}(Cl)\cdots Cu^{I}]^+$ (**3^{FeCl}**) – Abs$[(^6L)Fe^{II}(CO)\cdots Cu^{II}(Cl^{\bullet})]^+$ (**5**), Fig. 17b, indicating the product is **3^{FeCl}**, Scheme 8. Remarkably, the generation of this state could not be time-resolved with our apparatus. This indicates that chlorine atom transfer from copper to iron occurs with a rate constant >10^8 s^{-1}! This rapid rate supports the notion suggested by the stopped-flow kinetic measurements that atom transfer occurs through an inner-sphere mechanism with a bridging chloride intermediate.

On a 100 μs time scale (k_2), the photogenerated intermediate $[(^6L)Fe^{III}(Cl)\cdots Cu^{I}]^+$ (**3^{FeCl}**) returns to a product that contains the heme carbonyl. The spectral data were fully consistent with transfer of the chlorine atom back to the copper center, however the strong absorbance of the heme did not allow us to directly monitor the coordination of the copper center. Thus, an electron-/atom- ($Cl^{\bullet}$) transfer process takes place within an observed rate (k_2) of ~10^3 s^{-1}. Given that acetonitrile is a poor ligand for Cu(II), k_2 (Scheme 8) is comprised of electron-/atom- ($Cl^{\bullet}$) transfer coupled with CO rebinding, this observed rate constant does not correspond solely to single chlorine atom transfer and cannot be directly compared to the related Cl˙ transfer process of the monomeric $[Cu^I(tmpa)(CH_3CN)]^+$ ($^{\mathbf{tmpa}}\mathbf{2}$)/$[(F_8)Fe^{III}(Cl)]$ (**1′-Cl**) analogue. Nevertheless, we predict that the rate of electron-/atom- (Cl˙) transfer from $[(^6L)Fe^{III}(Cl)\cdots Cu^I]^+$ ($\mathbf{3^{FeCl}}$) to form $[(^6L)Fe^{II}\cdots Cu^{II}(Cl)]^+$ ($\mathbf{3^{CuCl}}$) would exceed the corresponding value for the ($^{\mathbf{tmpa}}\mathbf{2}$)/(**1′-Cl**) reaction. Based on the trend in k_{obs} for the $[LCu^I]^+/[(F_8)Fe^{II}]$ system as obtained by stopped-flow UV–Vis spectroscopy in relation to the $[LCu^{II}(Cl)]^+$ τ values, copper ion moieties with square-based pyramidal geometries, as in $[(^6L)Fe^{II}\cdots Cu^{II}(Cl^\bullet)]^+$ ($\mathbf{3^{CuCl}}$), are expected to have higher electron-/atom- (Cl˙) transfer rates, *vide supra*.

4. Summary/conclusions

The reactions of $(F_8)Fe^{III}(Cl)$ (**1′-Cl**) with a series of $[(L)Cu^I]^+$ ($^{\mathbf{R}}\mathbf{2}$) complexes (L = TMPA, PMEA, PMAP) lead to electron-/atom- (Cl˙) transfer chemistry, giving $(F_8)Fe^{II}$ (**1**) and $[(L)Cu^{II}(Cl)]^+$ ($^{\mathbf{R}}\mathbf{2'}$**-Cl**). For $[Cu^I(tepa)]^+$ ($^{\mathbf{tepa}}\mathbf{2}$), a reaction with $(F_8)Fe^{III}(Cl)$ (**1′-Cl**) does not occur due to unfavorable thermodynamics. Stopped-flow spectroscopy indicates that $(F_8)Fe^{III}(Cl)$ (**1′-Cl**) oxidizes the $[(L)Cu^I]^+$ ($^{\mathbf{R}}\mathbf{2}$) complexes in THF solvent with the following trend in relative rates $[Cu^I(pmea)]^+$ ($^{\mathbf{pmea}}\mathbf{2}$) > $[Cu^I(pmap)]^+$ ($^{\mathbf{pmap}}\mathbf{2}$) > $[Cu^I(tmpa)(CH_3CN)]^+$ ($^{\mathbf{tmpa}}\mathbf{2}$). Redox potentials predict a differing trend, $[Cu^I(tmpa)(CH_3CN)]^+$ ($^{\mathbf{tmpa}}\mathbf{2}$) > $[Cu^I(pmea)]^+$ ($^{\mathbf{pmea}}\mathbf{2}$) > $[Cu^I(pmap)]^+$ ($^{\mathbf{pmap}}\mathbf{2}$), where the relative driving force was estimated by calculating $E_{1/2}(\text{oxidant}) - E_{1/2}(\text{reductant})$. Thus, the results point to a likely inner-sphere mechanism for Cl˙ transfer from heme to copper.

The study of $[(^6L)Fe\cdots(Cl)\cdots Cu]^+$ (**3**) as an analog to the pairing of the mononuclear species $(F_8)Fe^{III}(Cl)$ (**1′-Cl**) and $[Cu^I(tmpa)(CH_3CN)]^+$ ($^{\mathbf{tmpa}}\mathbf{2}$) results in an interesting equilibrium between $[(^6L)Fe^{III}(Cl)\cdots Cu^I]^+$ ($\mathbf{3^{FeCl}}$) and $[(^6L)Fe^{II}\cdots Cu^{II}(Cl)]^+$ ($\mathbf{3^{CuCl}}$). This equilibrium is displayed as nearly 1:1 ($\mathbf{3^{FeCl}}$):($\mathbf{3^{CuCl}}$) by ^{1}H NMR (THF-d_8) and electrochemical studies (CH_3CN). Upon addition of an axial base like pyridine or 1,5-DCHIm, the equilibrium shifts towards $\mathbf{3^{CuCl}}$ accompanied by ‘base’ binding to iron(II). Adding carbon monoxide similarly results in an equilibrium shift towards $[(^6L)Fe^{II}(CO)\cdots Cu^{II}(Cl)]^+$ (**5**). Upon photolysis of **5**, we generate $\mathbf{3^{CuCl}}$ which competitively rebinds CO or undergoes an assumed electron-/atom- (Cl˙) transfer process forming $\mathbf{3^{FeCl}}$. Ultimately, $\mathbf{3^{FeCl}}$ equilibrates back to **5** in an overall reversible process. Quantifying the kinetics was difficult due to the composite nature of the reaction.

In conclusion, electron-/atom- (Cl˙) transfer reactions have been observed in systems involving a combination of heme and copper ion centers, in both inter- and intramolecular cases. Based on the lack of correlation of reaction rates and thermodynamic factors, the occurrence of an inner-sphere chloride-bridged intermediate is suggested although it is not observed. The details of bond-breaking and bond-making along with electronic coupling across the chloride bridge are likely to be important considerations. Further, we suggest that significant contributions to the observed behavior will come from copper ion structural changes occurring during the redox reactions, but differing for the various copper–ligand complexes. Ligand effects on outer-versus inner-sphere oxidations of (ligand)-Cu(I) complexes have been recently probed by Meyerstein and colleagues [53]. Further studies on the present or newly designed systems will be of interest and required to provide additional insights.

Acknowledgements

We are very grateful for financial support of this research (K.D.K., National Institutes of Health, GM28962 and GM60353; G.J.M., National Science Foundation, CHE 0616500).

Appendix A. Supplementary material

CCDC 657126 contain the supplementary crystallographic data for this paper. These data can be obtained free of charge via http://www.ccdc.cam.ac.uk/conts/retrieving.html, or from the Cambridge Crystallographic Data Centre, 12 Union Road, Cambridge CB2 1EZ, UK; fax: (+44) 1223-336-033; or e-mail: deposit@ccdc.cam.ac.uk. Supplementary data associated with this article can be found, in the online version, at doi:10.1016/j.ica.2007.08.016.

References

[1] E.E. Chufán, S.C. Puiu, K.D. Karlin, Acc. Chem. Res. 40 (2007) 563.

[2] R.A. Ghiladi, E.E. Chufan, D. delRio, E.I. Solomon, C. Krebs, B.H. Huynh, H.w. Huang, P. Moenne-Loccoz, S. Kaderli, M. Honecker, A.D. Zuberbuhler, L. Marzilli, R.J. Cotter, K.D. Karlin, Inorg. Chem. 46 (2007) 3889.

[3] R.A. Ghiladi, H.W. Huang, P. Moënne-Loccoz, J. Stasser, N.J. Blackburn, A.S. Woods, R.J. Cotter, C.D. Incarvito, A.L. Rheingold, K.D. Karlin, J. Biol. Inorg. Chem. 10 (2005) 63.

[4] E. Kim, E.E. Chufán, K. Kamaraj, K.D. Karlin, Chem. Rev. 104 (2004) 1077.

[5] J.P. Collman, R. Boulatov, C.J. Sunderland, L. Fu, Chem. Rev. 104 (2004) 561.

[6] H.C. Fry, A.D. Cohen, J.P. Toscano, G.J. Meyer, K.D. Karlin, J. Am. Chem. Soc. 127 (2005) 6225.

[7] R.M. Kretzer, R.A. Ghiladi, E.L. Lebeau, H.-C. Liang, K.D. Karlin, Inorg. Chem. 42 (2003) 3016.

[8] D.W. Thompson, R.M. Kretzer, E.L. Lebeau, D.V. Scaltrito, R.A. Ghiladi, K.-C. Lam, A.L. Rheingold, K.D. Karlin, G.J. Meyer, Inorg, Chem. 42 (2003) 5211.

[9] A. Nanthakumar, S. Fox, K.D. Karlin, J. Chem. Soc., Chem. Commun. (1995) 499.

[10] D.B. Rorabacher, Chem. Rev. 104 (2004) 651.

[11] M. Schatz, M. Becker, F. Thaler, F. Hampel, S. Schindler, R.R. Jacobson, Z. Tyeklár, N.N. Murthy, P. Ghosh, Q. Chen, J. Zubieta, K.D. Karlin, Inorg. Chem. 40 (2001) 2312.

[12] K.D. Karlin, J.C. Hayes, J. Shi, J.P. Hutchinson, J. Zubieta, Inorg. Chem. 21 (1982) 4106.

[13] R.A. Ghiladi, T.D. Ju, D.-H. Lee, P. Moënne-Loccoz, S. Kaderli, Y.-M. Neuhold, A.D. Zuberbühler, A.S. Woods, R.J. Cotter, K.D. Karlin, J. Am. Chem. Soc. 121 (1999) 9885.

[14] E. Kim, M.E. Helton, S. Lu, P. Moënne-Loccoz, C.D. Incarvito, A.L. Rheingold, S. Kaderli, A.D. Zuberbühler, K.D. Karlin, Inorg. Chem. 44 (2005) 7014.

[15] C.X. Zhang, H.-C. Liang, E.-i. Kim, J. Shearer, M.E. Helton, E. Kim, S. Kaderli, C.D. Incarvito, A.D. Zuberbühler, A.L. Rheingold, K.D. Karlin, J. Am Chem. Soc. 125 (2003) 634.

[16] H.C. Fry, H.R. Lucas, A.A. Narducci Sarjeant, G.J. Meyer, K.D. Karlin, submitted for publication.

[17] R.A. Ghiladi, R.M. Kretzer, I. Guzei, A.L. Rheingold, Y.-M. Neuhold, K.R. Hatwell, A.D. Zuberbühler, K.D. Karlin, Inorg. Chem. 40 (2001) 5754.

[18] C.A. Bignozzi, R. Argazzi, C. Chiorboli, F. Scandola, R.B. Dyer, J.R. Schoonover, T.J. Meyer, Inorg. Chem. 33 (1994) 1652.

[19] H.C. Fry, D.V. Scaltrito, K.D. Karlin, G.J. Meyer, J. Am Chem. Soc. 125 (2003) 11866.

[20] C.X. Zhang, S. Kaderli, M. Costas, E.-i. Kim, Y.-M. Neuhold, K.D. Karlin, A.D. Zuberbühler, Inorg. Chem. 42 (2003) 1807.

[21] P. van der Sluis, A.L. Spek, Acta Cyrstallogr., Sect. A 46 (1990) 194.

[22] H.-C. Liang, E. Kim, C.D. Incarvito, A.L. Rheingold, K.D. Karlin, Inorg. Chem. 41 (2002) 2209.

[23] W.R. Scheidt, C.A. Reed, Chem. Rev. 81 (1981) 543.

[24] F.A. Walker, U. Simonis, in: R.B. King (Ed.), Encyclopedia of Inorganic Chemistry, 2nd ed., John Wiley & Sons Ltd., 2005, p. 2390.

[25] Z. Tyeklár, R.R. Jacobson, N. Wei, N.N. Murthy, J. Zubieta, K.D. Karlin, J. Am. Chem. Soc. 115 (1993) 2677.

[26] R.R. Jacobson, Dissertation, State University of New York at Albany, 1989.

[27] A.W. Addison, T.N. Rao, J. Reedijk, J. van Rijn, G.C. Verschoor, J. Chem. Soc., Dalton Trans. (1984) 1349.

[28] N. Wei, N.N. Murthy, K.D. Karlin, Inorg. Chem. 33 (1994) 6093.

[29] B. Lucchese, K.J. Humphreys, D.-H. Lee, C.D. Incarvito, R.D. Sommer, A.L. Rheingold, K.D. Karlin, Inorg. Chem. 43 (2004) 5987.

[30] D.N. Hendrickson, M.G. Kinnaird, K.S. Suslick, J. Am. Chem. Soc. 109 (1987) 1243.

[31] H.-C. Liang, K.D. Karlin, R. Dyson, S. Kaderli, B. Jung, A.D. Zuberbühler, Inorg. Chem. 39 (2000) 5884.

[32] R.A. Ghiladi, K.D. Karlin, Inorg. Chem. 41 (2002) 2400.

[33] I.M. Wasser, H.W. Huang, P. Moenne-Loccoz, K.D. Karlin, J. Am. Chem. Soc. 127 (2005) 3310.

[34] E. Kim, M.E. Helton, I.M. Wasser, K.D. Karlin, S. Lu, H.-w. Huang, P. Moënne-Loccoz, C.D. Incarvito, A.L. Rheingold, M. Honecker, S. Kaderli, A.D. Zuberbühler, Proc. Natl. Acad. Sci. USA 100 (2003) 3623.

[35] B.S. Lim, R.H. Holm, Inorg. Chem. 37 (1998) 4898.

[36] D. Lancon, K.M. Kadish, J. Am. Chem. Soc. 105 (1983) 5610.

[37] G. Balducci, G. Chottard, C. Gueutin, D. Lexa, J.M. Saveant, Inorg. Chem. 33 (1994) 1972.

[38] K.M. Kadish, E. Van Caemelbecke, F. D'Souza, M. Lin, D.J. Nurco, C.J. Medforth, T.P. Forsyth, B. Krattinger, K.M. Smith, S. Fukuzumi, I. Nakanishi, J.A. Shelnutt, Inorg. Chem. 38 (1999) 2188.

[39] N. Wei, N.N. Murthy, Q. Chen, J. Zubieta, K.D. Karlin, Inorg. Chem. 33 (1994) 1953.

[40] R. Boulatov, J.P. Collman, I.M. Shiryaeva, C.J. Sunderland, J. Am. Chem. Soc. 124 (2002) 11923.

[41] J.P. Collman, Y.L. Yan, J. Lei, P.H. Dinolfo, Inorg. Chem. 45 (2006) 7581.

[42] J.P. Collman, N.K. Devaraj, R.A. Decreau, Y. Yang, Y.-L. Yan, W. Ebina, T.A. Eberspacher, C.E.D. Chidsey, Science 315 (2007) 1565.

[43] D. Rehm, A. Weller, Isr. J. Chem. 8 (1970) 259.

[44] M. Chou, C. Creutz, N. Sutin, J. Am. Chem. Soc. 99 (1977) 5615.

[45] R.A. Marcus, N. Sutin, Biochim. Biophys. Acta 811 (1985) 265.

[46] C. Creutz, P.C. Ford, T.J. Meyer, Inorg. Chem. 45 (2006) 7059.

[47] A. Haim, Prog. Inorg. Chem. 30 (1983) 273.

[48] M.Y. Udugala-Ganehenege, M.J. Heeg, L.M. Hryhorczuk, L.E. Wenger, J.F. Endicott, Inorg. Chem. 40 (2001) 1614.

[49] J.F. Endicott, M.J. Uddin, Coord. Chem. Rev. 219 (2001) 687.

[50] E. Antonini, M. Brunori, Hemoglobin and Myoglobin in Their Reactions, North-Holland Publishing Co., Amsterdam, 1971.

[51] T.G. Traylor, Acc. Chem. Res. 14 (1981) 102.

[52] D. Toptygin, A.M. Gronenborn, L. Brand, J. Phys. Chem. B 110 (2006) 26292.

[53] A. Burg, E. Maimon, H. Cohen, D. Meyerstein, Eur. J. Inorg. Chem. (2007) 530.